

# XLPR MODELS SUBGROUP REPORT

CRACK TRANSITION



**PROBABILISTIC FRACTURE MECHANICS CODE**

## **DISCLAIMER**

THIS PUBLICATION WAS PREPARED AS AN ACCOUNT OF WORK JOINTLY SPONSORED BY THE ELECTRIC POWER RESEARCH INSTITUTE (EPRI) AND AN AGENCY OF THE U.S. GOVERNMENT. NEITHER EPRI NOR THE U.S. GOVERNMENT NOR ANY AGENCY THEREOF, NOR ANY EMPLOYEE OF ANY OF THE FOREGOING, MAKES ANY WARRANTY, EXPRESSED OR IMPLIED, OR ASSUMES ANY LEGAL LIABILITY OR RESPONSIBILITY FOR ANY THIRD PARTY'S USE, OR THE RESULTS OF SUCH USE, OF ANY INFORMATION, APPARATUS, PRODUCT, OR PROCESS DISCLOSED IN THIS PUBLICATION, OR REPRESENTS THAT ITS USE BY SUCH THIRD PARTY COMPLIES WITH APPLICABLE LAW.

EPRI RETAINS COPYRIGHT IN EPRI-GENERATED MATERIALS CONTAINED IN THIS PUBLICATION.

THIS PUBLICATION DOES NOT CONTAIN OR IMPLY LEGALLY BINDING REQUIREMENTS. NOR DOES THIS PUBLICATION ESTABLISH OR MODIFY ANY REGULATORY GUIDANCE OR POSITIONS OF THE U.S. NUCLEAR REGULATORY COMMISSION AND IS NOT BINDING ON THE COMMISSION.

**xLPR Models Subgroup Report**  
**Crack Transition**

**xLPR-MSGR-CTM Version 1.0**

<b>Author Signature</b>	<b>Date</b>
Do Jun Shim Do Jun Shim, Structural Integrity Associates Lead, Crack Transition Subgroup	04/07/16
<b>Reviewer Signatures</b>	<b>Date</b>
Jay Wallace Jay Wallace, Nuclear Regulatory Commission Member, Crack Transition Subgroup	04/07/16
<b>Approver Signatures</b>	<b>Date</b>
Marjorie Erickson Marjorie Erickson, PEAI xLPR Models Group Lead	04/07/16
Craig D. Harrington Craig D. Harrington, Electric Power Research Institute xLPR Code Development Lead	04/20/16

THE TECHNICAL CONTENTS OF THIS DOCUMENT WERE NOT PREPARED IN  
ACCORDANCE WITH THE XLPR SOFTWARE QUALITY ASSURANCE PLAN.

## Revision History

Version Number	Description of Changes	Issue Date
1.0	Initial Issue	04/20/2016
	The U.S. Nuclear Regulatory Commission Office of Nuclear Regulatory Research's and the Electric Power Research Institute's xLPR Project Contacts approved an administrative update in 2021 to support public release of this document without incrementing the version number or issue date. The administrative updates included: (a) title changed from "Surface-to-Through-Wall Crack Transition Module Development for xLPR Version 2.0" to "xLPR Models Subgroup Report—Crack Transition" throughout the document, (b) cover and title pages updated accordingly, (c) disclaimer statement added, and (d) statement that the document was not prepared in accordance with the xLPR Software Quality Assurance Plan added.	

## **EXECUTIVE SUMMARY**

For typical leak-before-break (LBB) analysis, an idealized through-wall crack (TWC) is postulated (i.e., crack front parallel to the cylinder radius for circumferential TWC and crack front perpendicular to the wall thickness direction for axial TWC). Such an assumption simplifies the analysis significantly. However, recent studies have shown that a subcritical surface crack (SC), due to primary water stress corrosion cracking (PWSCC), can transition to a TWC with significant differences between the inner diameter (ID) and outer diameter (OD) crack lengths (i.e., non-idealized TWC or transition crack). Similar results have been observed experimentally in fatigue pipe tests.

In practical LBB applications, it is assumed that an idealized TWC is formed once the SC penetrates the wall thickness. For example, in Version 1.0 of the xLPR code, the length of the idealized circumferential TWC is determined by assuming that the TWC has the equivalent crack area as the SC at leakage. This type of crack transition was selected since no general stress intensity factor (K) and crack-opening displacement (COD) solutions were available for crack shapes that would form during the transitioning stages, i.e., non-idealized TWC. However, it has been demonstrated that this crack transition method may provide non-conservative results in terms of leak rate calculations. Thus, it was necessary to further investigate this issue and develop a model that can handle the SC to TWC transition more accurately.

In xLPR Version 2.0, a SC to TWC transition model has been developed using K and COD solutions for both circumferential and axial non-idealized TWCs. The K and COD values for non-idealized TWCs were represented by applying correction factors to those of idealized TWCs with the same ID crack size. This model determines when the transition should occur (based on surface crack depth) and determines the two crack lengths (at ID and OD surfaces) of the initial non-idealized TWC. Furthermore, growth of the non-idealized TWC can be calculated using the corrected K values defined by the proposed model.

The xLPR Ver. 2.0 Crack Transition (CT) Module implements this crack transition model. The module was developed according to the CT Software Requirements Description (SRD) and Software Design Descriptions (SDD). Verification of the CT Module was carried out according to the CT Software Test Plan (STP). Verification that the CT Module satisfies the requirements specified in the CT SRD is documented in detail in the CT Software Test Result Report (STRR).

Finally, the CT Module was validated by comparing the crack growth calculation results with published experimental data from the literature. The CT Module and K Modules were used to simulate fatigue crack growth of circumferential cracks in pipes under bending loads to the point of wall penetration and through the TWC transition stage until idealized TWCs were formed. The validation was focused on the crack shape evolution during crack growth predicted using the crack transition-corrected K values. The crack sizes/shapes from the validation dataset formed during crack growth were well captured by the xLPR modules. This also validated that the crack shapes used in xLPR (i.e., semi-elliptical surface crack, non-idealized through-wall crack, and idealized through-wall crack) are sufficient to represent the crack shapes formed during laboratory pipe fatigue tests. Furthermore, the calculation results demonstrated that the crack shape evolution is independent of fatigue crack growth rate, which validated the accuracy of the K-solutions.

## TABLE OF CONTENTS

<b>EXECUTIVE SUMMARY .....</b>	<b>IV</b>
<b>TABLE OF CONTENTS .....</b>	<b>V</b>
<b>TABLE OF FIGURES .....</b>	<b>VI</b>
<b>TABLE OF TABLES .....</b>	<b>VII</b>
<b>NOMENCLATURE/LIST OF SYMBOLS .....</b>	<b>VIII</b>
<b>ACRONYMS AND INITIALISMS .....</b>	<b>X</b>
<b>1. INTRODUCTION.....</b>	<b>1</b>
1.1 Subgroup Roles and Responsibilities .....	1
1.2 Subgroup Objectives.....	2
1.3 Models Under Auspices of Subgroup .....	3
<b>2. CRACK TRANSITION MODEL .....</b>	<b>4</b>
2.1 Model Description .....	4
2.2 K and COD Correction Factors for Non-Idealized TWCs.....	6
2.2.1 Circumferential Crack .....	6
2.2.2 Axial Crack .....	21
2.3 Crack Transition Model .....	32
<b>3. MODULE DEVELOPMENT .....</b>	<b>34</b>
3.1 Module Requirements.....	34
3.2 Module Inputs and Outputs.....	38
3.3 Module Verification and Validation.....	40
3.3.1 CT Module Verification .....	40
3.3.2 CT Module Validation .....	41
3.4 Module Limitations .....	48
<b>4. RECOMMENDATIONS FOR VERSION 3.0 MODIFICATIONS .....</b>	<b>50</b>
<b>5. LESSONS LEARNED.....</b>	<b>51</b>
<b>6. SUMMARY.....</b>	<b>52</b>
<b>7. REFERENCES.....</b>	<b>53</b>

## TABLE OF FIGURES

Figure 1.	Transition from surface crack to through-wall crack assuming equivalent crack area .....	4
Figure 2.	Schematic illustration of the crack transition model for (a) circumferential crack and (b) axial crack in pipe .....	5
Figure 3.	Dimensions of non-idealized circumferential through-wall crack.....	6
Figure 4.	Example FE mesh of non-idealized circumferential through-wall crack used in past work ([5] and [7]) .....	6
Figure 5.	FE meshes used for the sensitivity study, (a) 15 elements, (b) 30 elements, (c) 60 elements, (d) 120 elements, (e) 180 elements along the TWC front.....	9
Figure 6.	Variation in G values along the TWC front for $R_m/t=5$ and $\sigma_1/\sigma=0.25$ - global bending, 180 elements along the crack front.....	9
Figure 7.	Sensitivity of G values to the number of element along the TWC front for $R_m/t=5$ and $\sigma_1/\sigma=0.25$ .....	10
Figure 8.	Sensitivity of H values to the number of elements along the TWC front for $R_m/t=5$ and $\sigma_1/\sigma=0.25$ .....	11
Figure 9.	G values for non-idealized circumferential TWCs in pipe ( $R_m/t=5$ ) under global bending.....	17
Figure 10.	H values for non-idealized circumferential TWCs in pipe ( $R_m/t=5$ ) under global bending.....	20
Figure 11.	Shape of non-idealized axial TWC assumed in [6].....	21
Figure 12.	Example FE mesh of non-idealized axial TWC obtained during natural crack growth.....	22
Figure 13.	AFEA results showing the natural crack front shapes obtained during crack transition.....	22
Figure 14.	Comparison of crack front shape (a) and K values (b) between straight and natural crack.....	23
Figure 15.	Representation of natural crack front shape using part of an ellipse for (a) crack shapes at early stage of crack transition and (b) for the entire crack transition ..	24
Figure 16.	Variation of shape functions (a) F and (b) $V_1$ and $V_2$ for idealized axial TWC under internal pressure.....	26
Figure 17.	Variation of correction factors ( $G_1$ and $G_2$ ) for non-idealized axial TWC under internal pressure ( $R_m/t=5$ ).....	30
Figure 18.	Variation of correction factors (a) $H_1$ and (b) $H_2$ for non-idealized axial TWC under internal pressure ( $R_m/t=5$ ).....	31
Figure 19.	Illustration of crack transition from SC to initial non-idealized TWC .....	33
Figure 20.	Idealized TWC (dashed line) used for calculation of K and COD for non-idealized TWC .....	33
Figure 21.	Crack growth calculation using K values at ID and OD surface points of non-idealized TWC .....	33
Figure 22.	(a) Flow Diagram of the Version 2.0 xLPR Crack Transition Module .....	36
Figure 23.	Example of fatigue fracture surfaces from Ref. [3] .....	42
Figure 24.	Fatigue crack growth rate versus SIF range from Ref. [3].....	42
Figure 25.	Comparison of surface crack growth .....	45
Figure 26.	Comparison of crack transition and through-wall crack growth .....	45
Figure 27.	Comparison of predicted and measured crack front shapes during crack growth (at random cycles) .....	46
Figure 28.	Comparison of number of cycles to wall penetration using FCGR from [3].....	46
Figure 29.	Comparison of number of cycles to wall penetration using optimized FCGR.....	47
Figure 30.	Effect of FCGR on crack growth and crack shape evolution .....	47
Figure 31.	Effect of plastic deformation on COD correction factor (H) values .....	48

## TABLE OF TABLES

Table 1.	Summary of pipe and crack geometries and loading conditions for circumferential crack.....	8
Table 2.	F, $V_1$ and $V_2$ values for idealized circumferential TWC under axial tension .....	14
Table 3.	F, $V_1$ and $V_2$ values for idealized circumferential TWC under global bending .....	14
Table 4.	$G_1$ values for non-idealized circumferential TWC under axial tension.....	15
Table 5.	$G_2$ values for non-idealized circumferential TWC under axial tension.....	15
Table 6.	$G_1$ values for non-idealized circumferential TWC under global bending .....	16
Table 7.	$G_2$ values for non-idealized circumferential TWC under global bending .....	16
Table 8.	$H_1$ values for non-idealized circumferential TWC under axial tension.....	18
Table 9.	$H_2$ values for non-idealized circumferential TWC under axial tension.....	18
Table 10.	$H_1$ values for non-idealized circumferential TWC under global bending .....	19
Table 11.	$H_2$ values for non-idealized circumferential TWC under global bending .....	19
Table 12.	F, $V_1$ and $V_2$ values for idealized axial TWC under internal pressure.....	27
Table 13.	$G_1$ values for non-idealized axial TWC under internal pressure.....	28
Table 14.	$G_2$ values for non-idealized axial TWC under internal pressure.....	28
Table 15.	$H_1$ values for non-idealized axial TWC under internal pressure .....	29
Table 16.	$H_2$ values for non-idealized axial TWC under internal pressure .....	29
Table 17.	SRD requirements for crack transition model.....	34
Table 18.	CT Module input parameters.....	38
Table 19.	CT Module output parameters.....	38
Table 20.	Error and warning flags used in the CT Module .....	39
Table 21.	Range limits for correction factors.....	39
Table 22.	Pipe geometry, initial surface crack size, loading condition, and fatigue life from experiments conducted by Yoo et al. ....	41
Table 23.	Summary of CT Model/Module assumptions and xLPR implications .....	49

## NOMENCLATURE/LIST OF SYMBOLS

### Symbols

A	Surface crack depth
$a_1$	Half crack length on the ID surface for non-idealized axial through-wall crack
$a_2$	Half crack length on the OD surface for non-idealized axial through-wall crack
$c_o$	Half crack length of final surface crack
$c'$	Half through-wall crack length determined from equivalent crack area method
$c_1^*$	Initial ID half crack length from circumferential crack transition
$c_2^*$	Initial OD half crack length from circumferential crack transition
cflag	Circumferential/Axial crack flag
E	Elastic modulus
F	Geometry factor in K solution for idealize through-wall crack
G1	Correction factor for K solution at ID surface
G2	Correction factor for K solution at OD surface
H1	Correction factor for COD solution at ID surface
H2	Correction factor for COD solution at OD surface
ierror	Error code output from the CT Module
K	Stress intensity factor
M	Global bending moment
N	Axial tension load
p	Internal pressure
R	Stress ratio (minimum stress/maximum stress for cyclic loading)
$R_i$	Inside pipe radius
$R_m$	Mean pipe radius
$R_o$	Outside pipe radius
t	Pipe wall thickness
$V_1$	COD shape function for idealized through-wall crack at ID surface
$V_2$	COD shape function for idealized through-wall crack at OD surface
$\square$	Distance from OD surface to ID surface
$\theta$	Half crack angle for circumferential through-wall crack
$\theta_1$	Half crack angle at ID surface
$\theta_2$	Half crack angle at OD surface
$\rho$	Normalized crack length for axial crack solutions
$\square_1$	Normalized crack length at ID surface
$\square_2$	Normalized crack length at OD surface

$\sigma$             Stress  
 $\nu$             Poisson's ratio

## **ACRONYMS AND INITIALISMS**

AFEA	Advanced Finite Element Analysis
ABAQUS	Finite Element Analysis Software
COD	Crack Opening Displacement
CT	Crack Transition
DLL	Dynamic Link Library
FCGR	Fatigue Crack Growth Rate
FEA	Finite Element Analysis
ID	Inside Diameter
KPW	K Part-Through Wall
KTW	K Though Wall
LBB	Leak-before-break
MVR	Module Validation Report
NRC	Nuclear Regulatory Commission
OD	Outside Diameter
PWSCC	Primary Water Stress Corrosion Cracking
RTC	Requirement Traceability Case
RTM	Requirements Traceability Matrix
SDD	Software Design Description
SIF	Stress Intensity Factor
SRD	Software Requirements Document
STP	Software Test Plan
STRR	Software Test Results Report
TWC	Through-Wall Crack
WRS	Weld Residual Stress
xLPR	eXtremely Low Probability of Rupture

## **1. INTRODUCTION**

### **1.1 Subgroup Roles and Responsibilities**

The Crack Transition (CT) subgroup within the xLPR Models Group was tasked with developing best-estimate surface crack (SC) to through-wall crack (TWC) transition models for both circumferentially and axially oriented cracks. The CT subgroup was also responsible for providing clear descriptions and appropriate quantification of all sources of uncertainty in model parameters, developing test cases for use in verifying and validating CT Module computer code performance, and accounting for model parameter and input value uncertainty. This subgroup was responsible for model documentation and working with the Computational Group to ensure proper performance of the CT Module within the xLPR Framework.

## **1.2 Subgroup Objectives**

The primary objectives of the CT Subgroup were:

- Define the analytical models necessary to predict the crack transition of circumferential and axial cracks.
- Develop\* the associated module (or software code) to perform the calculations.
- Define the necessary test cases for use in verifying and validating CT model computer code performance.
- Characterize model parameter and input value uncertainty.
- Produce CT Module documentation.
- 
- Interface with the Computational Group to ensure proper performance of the CT Module.

### **1.3 Models Under Auspices of Subgroup**

The CT models for circumferential and axial cracks were developed by the CT Subgroup. The CT Module determines the stress intensity factor (K) and crack opening displacement (COD) values for transition cracks by applying correction factors to the K and COD solutions for idealized TWCs. The idealized TWC solutions are addressed by other xLPR subgroups.

The correction factors were developed from linear elastic finite element (FE) analyses of transition cracks (i.e., non-idealized TWCs) in pipes. The CT subgroup was responsible for developing the FE analysis matrix, FE modeling, and determining the correction factors.

The CT Subgroup developed the transition criteria to determine the onset of the SC to TWC crack transition, size of the initial TWC, and termination of the crack transition. These transition criteria were provided to the Computational Group by the CT Subgroup.

## 2. CRACK TRANSITION MODEL

### 2.1 Model Description

Leak-before-break (LBB) analysis is an important fracture mechanics concept for design and integrity evaluation of pressurized nuclear piping. For typical LBB analysis, an idealized TWC is postulated (i.e., crack front parallel to the cylinder radius for circumferential TWC and crack front perpendicular to the wall thickness direction for axial TWC). Such an assumption simplifies the analysis significantly. However, recent studies [1, 2] have shown that a subcritical surface crack, due to primary water stress corrosion cracking (PWSCC), can transition to a TWC with significant differences between the inner diameter (ID) and outer diameter (OD) crack lengths (i.e., non-idealized TWC or transition crack). Similar results have been observed experimentally in fatigue pipe tests [3].

In typical LBB applications, it is assumed that an idealized TWC is formed once the surface crack penetrates the wall thickness. For example, in Version 1.0 of the xLPR code [4], the length of the idealized circumferential TWC is determined by assuming that the TWC has the equivalent crack area as the surface crack at leakage, as shown in Figure 1. The TWC length can be calculated by

$$c' = \frac{\pi c_o}{2} \frac{R_i}{R_o + R_i} \quad \text{s(Eq. 1)}$$

where  $R_i$  and  $R_o$  are the inner and outer radius, respectively.

This type of crack transition was selected since no general stress intensity factor ( $K$ ) and crack-opening displacement (COD) solutions were available for crack shapes that would form during the transitioning stages, i.e., non-idealized TWC. However, it has been demonstrated that this crack transition method may result in over prediction of the initial leakage rate, a non-conservative result for LBB analyses [2]. Thus, it was necessary to further investigate this issue and develop a model that can represent the SC to TWC transition more accurately.

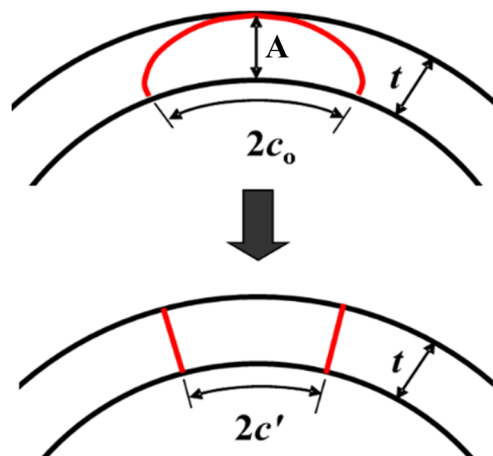


**Figure 1. Transition from surface crack to through-wall crack assuming equivalent crack area**

In the present CT model, a non-idealized TWC shape was introduced to more accurately capture the crack transition behavior. Figure 2 provides schematic illustration of the three crack types (i.e., semi-elliptical surface crack, non-idealized TWC, and idealized TWC in a pipe) involved in the CT model. The primary goal of the CT model was to develop correction factors to be applied to the K and COD solutions for idealized TWCs to calculate K and COD values for non-idealized TWCs that can be used to characterize the crack growth and leak-rate during the transitioning stage. Since only limited solutions were available [5, 6, 7], additional FE analyses were carried out to update and expand the correction factors for both circumferential and axial non-idealized TWCs [8, 9]. Note that the idealized TWC K and COD solutions are addressed by other xLPR subgroups.

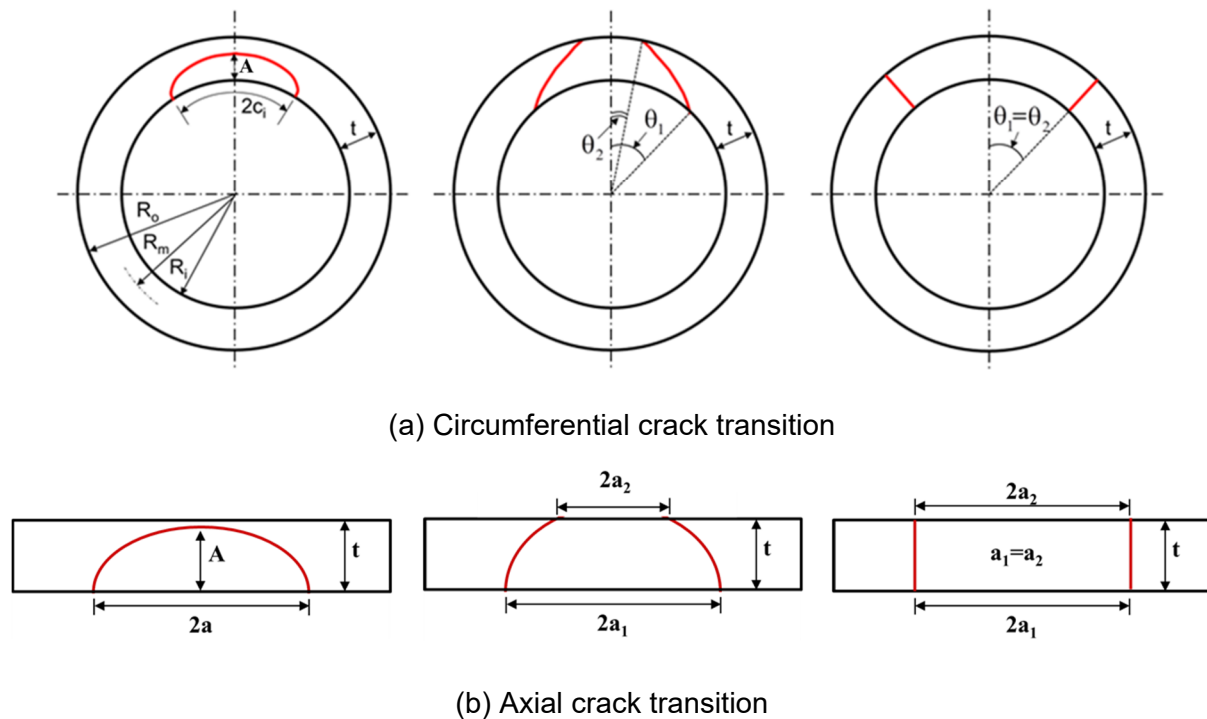


**Figure 2. Schematic illustration of the crack transition model for (a) circumferential crack and (b) axial crack in pipe**

As part of the CT model, the transition criteria to determine the onset of the SC-to-TWC crack transition, size of the initial TWC, and termination of the crack transition were provided for implementation within the xLPR Framework.

## 2.2 K and COD Correction Factors for Non-Idealized TWCs

### 2.2.1 Circumferential Crack

Limited K and COD solutions for circumferential non-idealized TWCs under simple loading conditions (i.e. global bending and axial tension) were published in [5] and [7]. These solutions are based on 3-dimensional (3D) elastic finite element (FE) analyses. Figure 3 shows a pipe with a non-idealized circumferential TWC, where  $R_m$  and  $t$  represent the mean radius and the thickness of the pipe, respectively. The non-idealized TWC is characterized by the half crack length (defined by half crack angle  $\theta_1$  and  $\theta_2$ ) on the inner and the outer surfaces of the pipe. There is some curvature along the crack front which is due to a cylindrical transformation of a straight crack front in a plate. Figure 4 shows an example mesh of a non-idealized circumferential TWC in a pipe from [5] and [7] where the bold solid line represents the crack front.

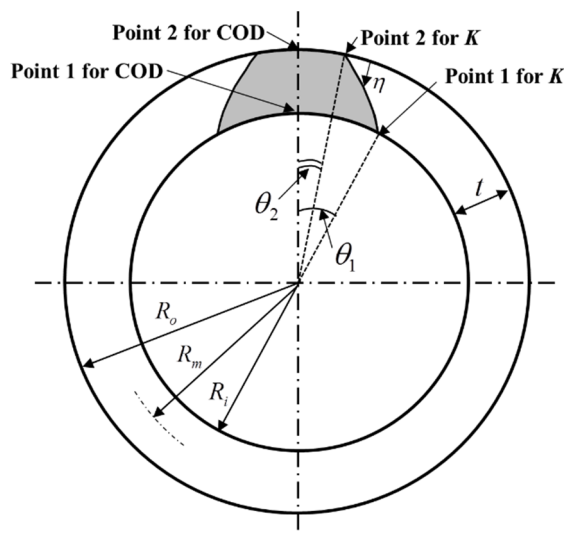


**Figure 3. Dimensions of non-idealized circumferential through-wall crack**

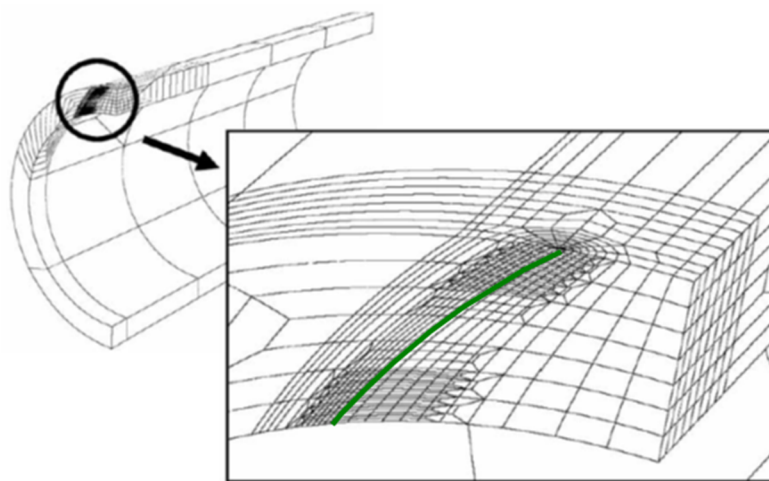


**Figure 4. Example FE mesh of non-idealized circumferential through-wall crack used in past work ([5] and [7])**

As described in [5] and [7], elastic FE calculations were conducted for limited pipe geometries ( $R_m/t$ ) and limited non-idealized circumferential TWC sizes for various loading conditions. The non-idealized TWC can be represented by two parameters, i.e.,  $\theta_1/\pi$  and  $\theta_1/\theta_2$ . The first parameter represents the crack length on the ID surface and the second parameter was used to determine the crack length on the OD surface. In [5] and [7], the  $\theta_1/\pi$  and  $\theta_1/\theta_2$  values ranged from 0.125 to 0.375 and 1 to 4, respectively. Note that when  $\theta_1/\theta_2=1$  the crack is an idealized TWC.

From the FE analyses of non-idealized TWC, the K values at the ID and OD surface points (Point 1 and Point 2 in Figure 3, respectively) were calculated. These values were represented using the following equations.

$$K_{I,ID}^{\text{Non-idealized}} = \sigma \sqrt{\pi R_m \theta_1} \cdot F \cdot G_1 = K_I^{\text{Idealized}} \cdot G_1 \quad (\text{Eq. 2})$$

$$K_{I,OD}^{\text{Non-idealized}} = \sigma \sqrt{\pi R_m \theta_1} \cdot F \cdot G_2 = K_I^{\text{Idealized}} \cdot G_2 \quad (\text{Eq. 3})$$

Here, the applied stress ( $\sigma$ ) is defined as,

$$\sigma = \frac{N}{2\pi R_m t} \quad \text{for axial tension (N)} \quad (\text{Eq. 4})$$

$$\sigma = \frac{M}{\pi R_m^2 t} \quad \text{for global bending (M)} \quad (\text{Eq. 5})$$

As shown in these equations, the  $G_1$  and  $G_2$  values are correction factors that are applied to the K value of an idealized TWC (with crack angle of  $\theta_1$ ) to obtain the K values at Point 1 and Point 2 of the non-idealized TWC. Note that K solutions for an idealized TWC, i.e., F values in Equations 2 and 3, are available in handbooks [10,11] and published literature [12].

Similarly, the COD values at the center of the crack at OD and ID surfaces were calculated from the FE analyses and were represented using the following equations.

$$\text{COD}_{ID}^{\text{Non-idealized}} = \frac{4\sigma R_m \theta_1}{E} \cdot V \cdot H_1 = \text{COD}^{\text{Idealized}} \cdot H_1 \quad (\text{Eq. 6})$$

$$\text{COD}_{OD}^{\text{Non-idealized}} = \frac{4\sigma R_m \theta_1}{E} \cdot V \cdot H_2 = \text{COD}^{\text{Idealized}} \cdot H_2 \quad (\text{Eq. 7})$$

where E is the elastic modulus. Here again, correction factors ( $H_1$  and  $H_2$ ) were multiplied by the COD value of the idealized TWC (with the crack angle of  $\theta_1$ ). Note that COD solutions for idealized TWC, i.e., V values in Equations 6 and 7, can be found in published literatures [10,13]. Note also that these V values are for the COD values at the mid-thickness of the pipe. Furthermore, note that a simple crack morphology with no engagement across the crack faces (unlike PWSCC) is assumed for these analyses.

As part of the xLPR Ver. 2.0 development, the existing K and COD solutions for non-idealized circumferential TWCs were updated and expanded. First, a mesh sensitivity study (which was not conducted in the previous work, [5] and [7]) was carried out to determine the appropriate mesh

size required to accurately calculate the K and COD values. Then, finite element analyses were performed to recalculate the correction factors for the non-idealized TWCs. In addition, the ranges of the solutions were expanded to cover more practical pipe geometries and crack sizes as summarized in Table 1.

**Table 1. Summary of pipe and crack geometries and loading conditions for circumferential crack**

Loading condition	$R_m/t$	$\theta_1/\pi$	$\theta_1/\theta_2$
Axial tension, Global bending	2, 5, 10, 20	0.125, 0.25, 0.3, 0.4, 0.5	1, 1.5, 2, 3, 4

For the mesh sensitivity study, the  $R_m/t$  and  $\theta_1/\pi$  values were fixed to 5 and 0.25, respectively. Three values of crack angle ratio ( $\theta_1/\theta_2$ ), 1, 2, and 4, were selected. The mesh sensitivity analysis was performed by varying the number of elements along the TWC front, from 15 to 180 elements. Figure 5 shows the FE meshes used for the sensitivity study where the view is focused near the TWC. Due to symmetry conditions, quarter models were employed. Reduced integration 20-node brick elements (element type C3D20R in ABAQUS element library) were used for the model. The crack-tip was modeled with a focused wedge type element with five contours. The elastic FE analyses were performed using the general purpose program ABAQUS [14], where the elastic modulus (E) and Poisson’s ratio ( $\nu$ ) were 190 GPa and 0.3, respectively. The K values were calculated along the crack front using the interaction integral method embedded within ABAQUS. The K value was determined as the mean value of 2nd~5th contours.

For the idealized TWCs ( $\theta_1/\theta_2 = 1$ ), the K values were averaged along the crack front to determine the F value in Equations 2 and 3. It was confirmed that the F values were not sensitive to the mesh size. Hence,  $G_1$  and  $G_2$  values are 1.0 for all idealized TWC cases. For the non-idealized TWCs, the G values vary along the crack front as illustrated in Figure 6. From these results, the  $G_1$  and  $G_2$  values were determined at the ID and OD surfaces. Figure 7 depicts the sensitivity of  $G_1$  and  $G_2$  values to the number of elements along the crack front. As the number of elements increased, the  $G_1$  values decreased and  $G_2$  values increased. Although a complete convergence of  $G_1$  values was not obtained, the changes in the values were relatively small and the absolute values were close to zero. On the other hand, the  $G_2$  values showed convergence when 180 elements were used along the crack front.

A similar sensitivity study for COD was also performed. In the present study, the V values for idealized TWCs were provided at the ID and OD surfaces as  $V_1$  and  $V_2$  (past work provided values at the mid-thickness location). Hence, Equations 6 and 7 can be rewritten as

$$COD_{ID}^{Non-idealized} = \frac{4\sigma R_m \theta_1}{E} \cdot V_1 \cdot H_1 = COD^{Idealized} \cdot H_1 \quad (Eq. 8)$$

$$COD_{OD}^{Non-idealized} = \frac{4\sigma R_m \theta_1}{E} \cdot V_2 \cdot H_2 = COD^{Idealized} \cdot H_2 \quad (Eq. 9)$$

Similar to the F values, the  $V_1$  and  $V_2$  values were not sensitive to the mesh size. Furthermore, the  $H_1$  and  $H_2$  values were independent of mesh size as demonstrated in Figure 8.

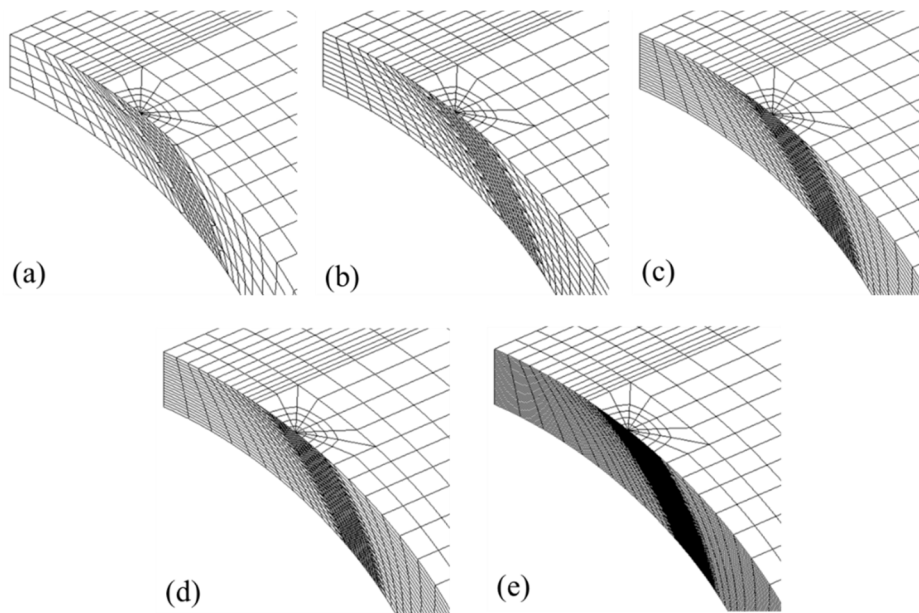


**Figure 5.** FE meshes used for the sensitivity study, (a) 15 elements, (b) 30 elements, (c) 60 elements, (d) 120 elements, (e) 180 elements along the TWC front

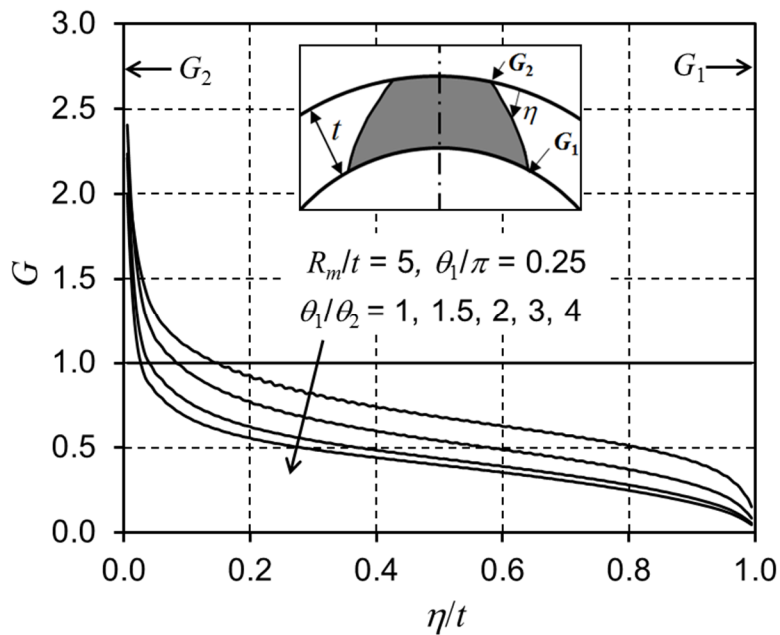
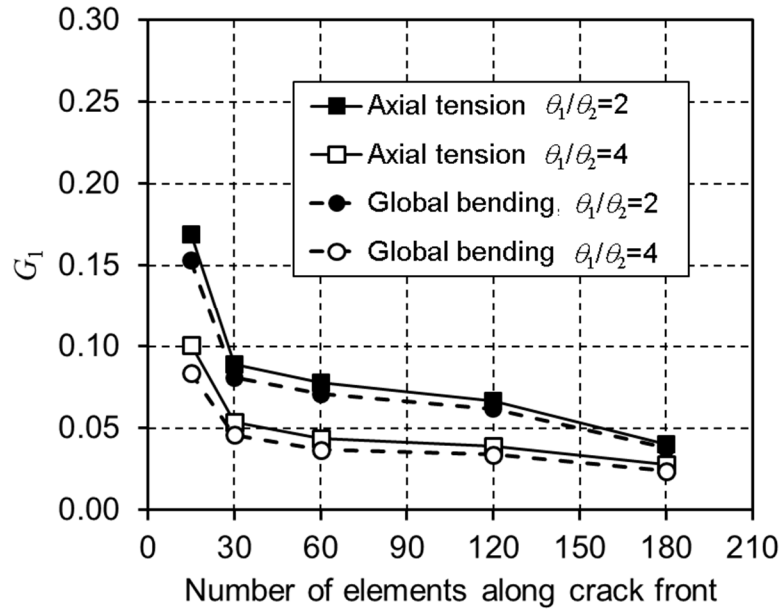
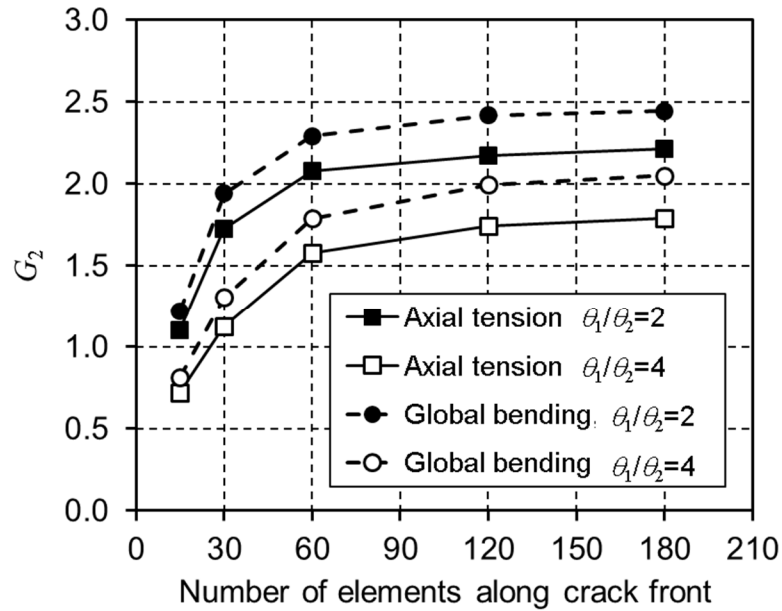


**Figure 6.** Variation in G values along the TWC front for  $R_m/t=5$  and  $\theta_1/\pi=0.25$  - global bending, 180 elements along the crack front



(a)  $G_1$  values



(b)  $G_2$  values

Figure 7. Sensitivity of G values to the number of element along the TWC front for  $R_m/t=5$  and  $\theta_1/\pi=0.25$

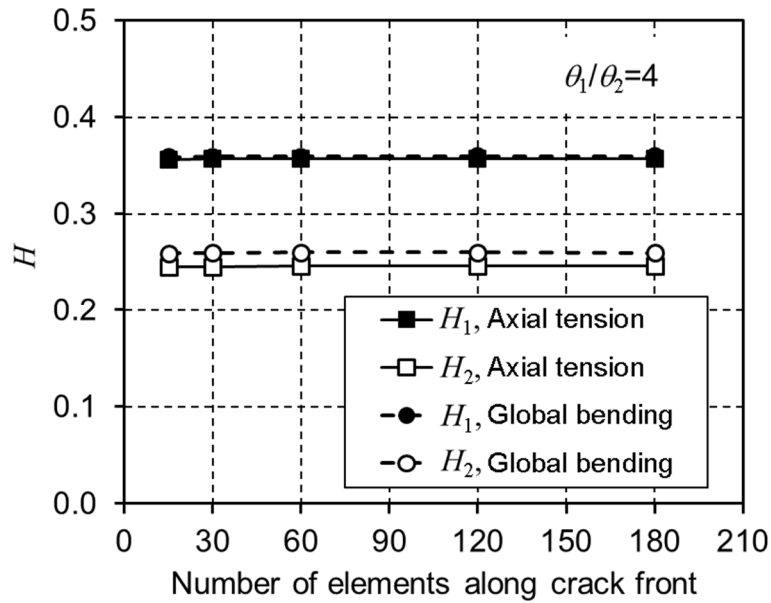
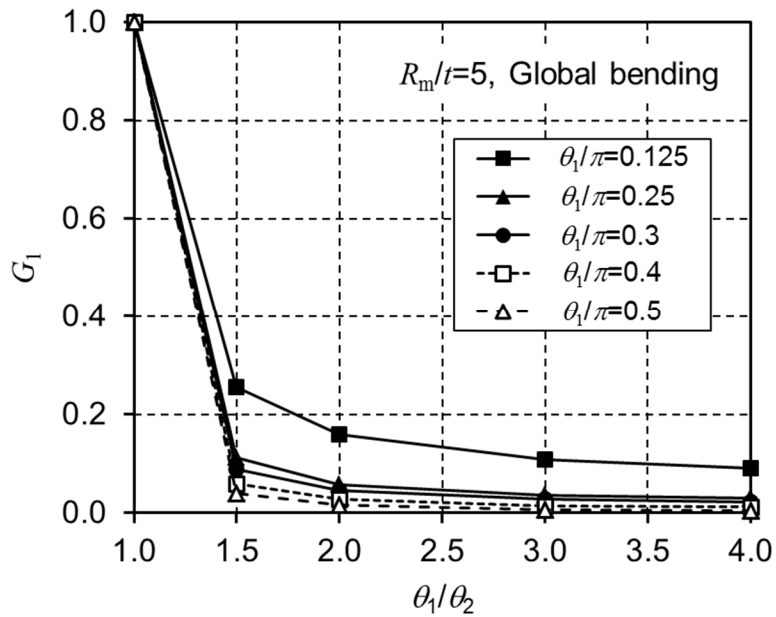


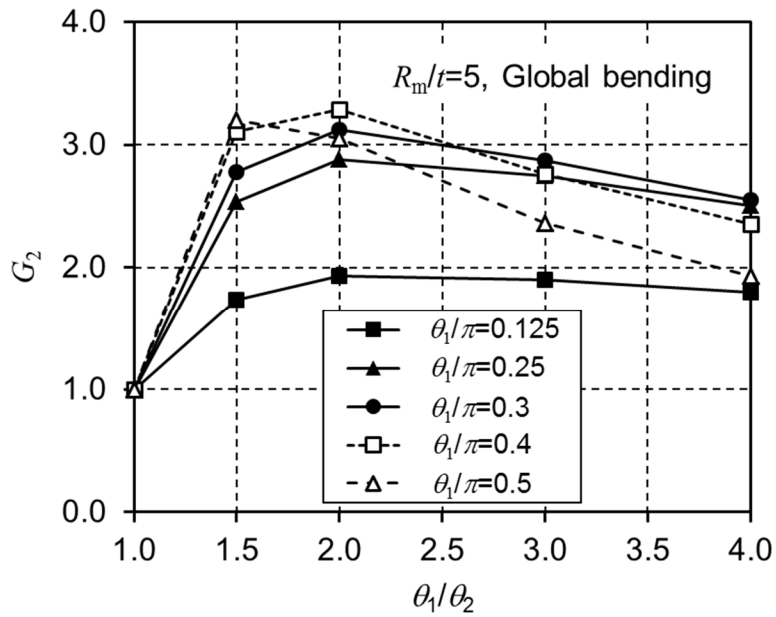
**Figure 8. Sensitivity of H values to the number of elements along the TWC front for  $R_m/t=5$  and  $\theta_1/\pi=0.25$**

Based on the sensitivity study results, FE analyses were conducted using the models with 180 elements along the crack front for all cases provided in Table 1. The  $F$ ,  $V_1$ , and  $V_2$  values for idealized TWC pipes under axial tension and global bending are provided in Table 2 and Table 3, respectively. Table 4 and Table 5 provide  $G_1$  and  $G_2$  values, respectively, for various non-idealized TWCs under axial tension and values for global bending are provided in Table 6 and Table 7. As provided in these tables, the  $G_2$  values are much greater than the  $G_1$  values indicating that the  $K$  values at Point 2 (OD surface) are significantly higher than the  $K$  values at Point 1 (ID surface) of a non-idealized TWCs. Figure 9 shows the trend of the  $G$  values for non-idealized TWCs in  $R_m/t=5$  pipe under global bending.

For COD, the  $H_1$  and  $H_2$  values for various non-idealized TWCs are provided in



(a) G1 values



(b) G2 values

Figure 9. G values for non-idealized circumferential TWCs in pipe ( $R_m/t=5$ ) under global bending

Table 8 and Table 9 for axial tension and Table 10 and Table 11 for global bending. Figure 10 shows the trends of the H values, where both  $H_1$  and  $H_2$  values decrease as the  $\theta_1/\theta_2$  value increases.

The updated K and COD (or G and H) solutions developed are employed in the crack transition model.

**Table 2. F, V<sub>1</sub> and V<sub>2</sub> values for idealized circumferential TWC under axial tension**

<b>R<sub>m</sub>/t</b>	<b>θ<sub>1</sub>/π</b>	<b>F</b>	<b>V<sub>1</sub></b>	<b>V<sub>2</sub></b>
2	0.125	1.163	0.882	1.412
	0.25	1.518	1.189	1.905
	0.3	1.738	1.429	2.247
	0.4	2.373	2.255	3.369
	0.5	3.407	3.963	5.630
5	0.125	1.226	0.999	1.404
	0.25	1.677	1.520	2.110
	0.3	1.935	1.901	2.559
	0.4	2.668	3.163	3.997
	0.5	3.872	5.747	6.895
10	0.125	1.315	1.108	1.527
	0.25	1.885	1.962	2.523
	0.3	2.188	2.540	3.140
	0.4	3.009	4.361	5.052
	0.5	4.352	7.906	8.770
20	0.125	1.458	1.315	1.763
	0.25	2.169	2.717	3.229
	0.3	2.525	3.586	4.098
	0.4	3.477	6.190	6.712
	0.5	5.021	11.105	11.708

**Table 3. F, V<sub>1</sub> and V<sub>2</sub> values for idealized circumferential TWC under global bending**

<b>R<sub>m</sub>/t</b>	<b>θ<sub>1</sub>/π</b>	<b>F</b>	<b>V<sub>1</sub></b>	<b>V<sub>2</sub></b>
2	0.125	1.080	0.719	1.477
	0.25	1.288	1.012	1.826
	0.3	1.405	1.207	2.071
	0.4	1.721	1.807	2.838
	0.5	2.201	2.912	4.265
5	0.125	1.178	0.947	1.418
	0.25	1.471	1.406	2.005
	0.3	1.620	1.715	2.356
	0.4	2.009	2.659	3.409
	0.5	2.607	4.404	5.349
10	0.125	1.270	1.080	1.521
	0.25	1.669	1.838	2.385
	0.3	1.852	2.315	2.885
	0.4	2.299	3.705	4.329
	0.5	2.976	6.146	6.872
20	0.125	1.411	1.291	1.744
	0.25	1.934	2.553	3.048
	0.3	2.155	3.281	3.768
	0.4	2.684	5.297	5.776
	0.5	3.472	8.722	9.241

**Table 4.  $G_1$  values for non-idealized circumferential TWC under axial tension**

$R_m/t$	$\theta_1/\pi$	$\theta_1/\theta_2$				
		1	1.5	2	3	4
2	0.125	1.000	0.556	0.471	0.399	0.367
	0.25	1.000	0.364	0.242	0.165	0.139
	0.3	1.000	0.311	0.187	0.118	0.096
	0.4	1.000	0.225	0.112	0.062	0.049
	0.5	1.000	0.159	0.066	0.034	0.026
5	0.125	1.000	0.276	0.174	0.119	0.101
	0.25	1.000	0.119	0.063	0.042	0.037
	0.3	1.000	0.093	0.050	0.033	0.029
	0.4	1.000	0.061	0.032	0.021	0.018
	0.5	1.000	0.041	0.020	0.012	0.011
10	0.125	1.000	0.091	0.071	0.062	0.058
	0.25	1.000	0.072	0.048	0.034	0.029
	0.3	1.000	0.064	0.039	0.026	0.023
	0.4	1.000	0.046	0.024	0.015	0.013
	0.5	1.000	0.030	0.013	0.008	0.007
20	0.125	1.000	0.068	0.063	0.048	0.043
	0.25	1.000	0.059	0.033	0.021	0.018
	0.3	1.000	0.047	0.024	0.015	0.013
	0.4	1.000	0.028	0.012	0.007	0.006
	0.5	1.000	0.014	0.005	0.003	0.003

**Table 5.  $G_2$  values for non-idealized circumferential TWC under axial tension**

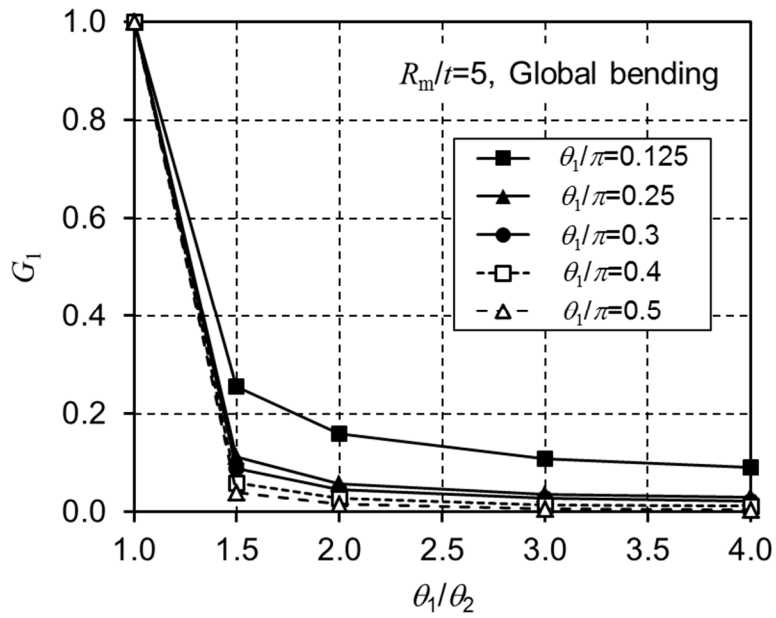
$R_m/t$	$\theta_1/\pi$	$\theta_1/\theta_2$				
		1	1.5	2	3	4
2	0.125	1.000	1.196	1.235	1.188	1.116
	0.25	1.000	1.513	1.627	1.564	1.461
	0.3	1.000	1.604	1.719	1.620	1.494
	0.4	1.000	1.717	1.780	1.578	1.402
	0.5	1.000	1.745	1.696	1.381	1.175
5	0.125	1.000	1.637	1.801	1.761	1.662
	0.25	1.000	2.343	2.592	2.424	2.188
	0.3	1.000	2.526	2.747	2.455	2.157
	0.4	1.000	2.733	2.737	2.201	1.847
	0.5	1.000	2.735	2.413	1.751	1.397
10	0.125	1.000	2.297	2.517	2.401	2.214
	0.25	1.000	3.206	3.366	2.849	2.425
	0.3	1.000	3.418	3.388	2.685	2.201
	0.4	1.000	3.538	3.030	2.100	1.629
	0.5	1.000	3.305	2.378	1.429	1.042
20	0.125	1.000	3.138	3.282	2.886	2.520
	0.25	1.000	3.884	3.417	2.408	1.898
	0.3	1.000	3.879	3.068	2.031	1.523
	0.4	1.000	3.481	2.241	1.263	0.947
	0.5	1.000	2.779	1.468	0.772	0.521

**Table 6.  $G_1$  values for non-idealized circumferential TWC under global bending**

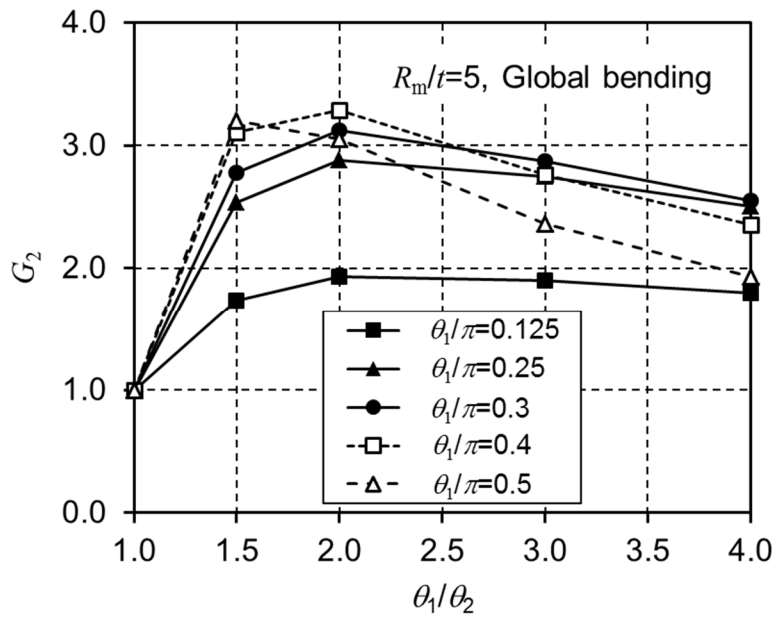
$R_m/t$	$\theta_1/\pi$	$\theta_1/\theta_2$				
		1	1.5	2	3	4
2	0.125	1.000	0.445	0.373	0.313	0.286
	0.25	1.000	0.314	0.200	0.130	0.106
	0.3	1.000	0.276	0.157	0.091	0.071
	0.4	1.000	0.211	0.096	0.045	0.032
	0.5	1.000	0.155	0.056	0.022	0.013
5	0.125	1.000	0.256	0.160	0.108	0.092
	0.25	1.000	0.113	0.058	0.037	0.031
	0.3	1.000	0.089	0.045	0.028	0.023
	0.4	1.000	0.060	0.028	0.015	0.012
	0.5	1.000	0.040	0.016	0.007	0.004
10	0.125	1.000	0.089	0.069	0.059	0.055
	0.25	1.000	0.070	0.045	0.030	0.025
	0.3	1.000	0.064	0.036	0.022	0.018
	0.4	1.000	0.046	0.021	0.010	0.008
	0.5	1.000	0.028	0.009	0.003	0.001
20	0.125	1.000	0.068	0.062	0.046	0.041
	0.25	1.000	0.059	0.031	0.018	0.015
	0.3	1.000	0.047	0.022	0.012	0.010
	0.4	1.000	0.026	0.009	0.004	0.003
	0.5	1.000	0.011	0.002	0.000	0.000

**Table 7.  $G_2$  values for non-idealized circumferential TWC under global bending**

$R_m/t$	$\theta_1/\pi$	$\theta_1/\theta_2$				
		1	1.5	2	3	4
2	0.125	1.000	1.384	1.446	1.408	1.333
	0.25	1.000	1.732	1.917	1.891	1.787
	0.3	1.000	1.844	2.055	2.002	1.874
	0.4	1.000	2.009	2.213	2.063	1.873
	0.5	1.000	2.082	2.198	1.921	1.685
5	0.125	1.000	1.738	1.929	1.901	1.802
	0.25	1.000	2.540	2.880	2.750	2.504
	0.3	1.000	2.778	3.124	2.871	2.551
	0.4	1.000	3.105	3.285	2.760	2.358
	0.5	1.000	3.201	3.055	2.363	1.935
10	0.125	1.000	2.376	2.621	2.518	2.328
	0.25	1.000	3.416	3.671	3.166	2.715
	0.3	1.000	3.703	3.793	3.082	2.552
	0.4	1.000	3.980	3.596	2.598	2.049
	0.5	1.000	3.855	2.996	1.916	1.431
20	0.125	1.000	3.209	3.379	2.987	2.615
	0.25	1.000	4.106	3.696	2.650	2.103
	0.3	1.000	4.175	3.408	2.312	1.749
	0.4	1.000	3.900	2.647	1.554	1.185
	0.5	1.000	3.240	1.848	1.035	0.715



(a)  $G_1$  values



(b)  $G_2$  values

Figure 9. G values for non-idealized circumferential TWCs in pipe ( $R_m/t=5$ ) under global bending

**Table 8.  $H_1$  values for non-idealized circumferential TWC under axial tension**

$R_m/t$	$\theta_1/\pi$	$\theta_1/\theta_2$				
		1	1.5	2	3	4
2	0.125	1.000	0.876	0.822	0.773	0.749
	0.25	1.000	0.721	0.611	0.525	0.490
	0.3	1.000	0.660	0.531	0.435	0.397
	0.4	1.000	0.546	0.391	0.285	0.248
	0.5	1.000	0.442	0.277	0.176	0.144
5	0.125	1.000	0.819	0.737	0.663	0.629
	0.25	1.000	0.653	0.510	0.400	0.357
	0.3	1.000	0.600	0.440	0.323	0.280
	0.4	1.000	0.505	0.328	0.210	0.170
	0.5	1.000	0.411	0.236	0.132	0.099
10	0.125	1.000	0.760	0.651	0.558	0.518
	0.25	1.000	0.595	0.427	0.304	0.258
	0.3	1.000	0.551	0.372	0.245	0.199
	0.4	1.000	0.473	0.286	0.163	0.122
	0.5	1.000	0.388	0.212	0.107	0.074
20	0.125	1.000	0.686	0.548	0.439	0.395
	0.25	1.000	0.547	0.361	0.227	0.179
	0.3	1.000	0.513	0.322	0.188	0.141
	0.4	1.000	0.446	0.258	0.134	0.092
	0.5	1.000	0.365	0.194	0.092	0.059

**Table 9.  $H_2$  values for non-idealized circumferential TWC under axial tension**

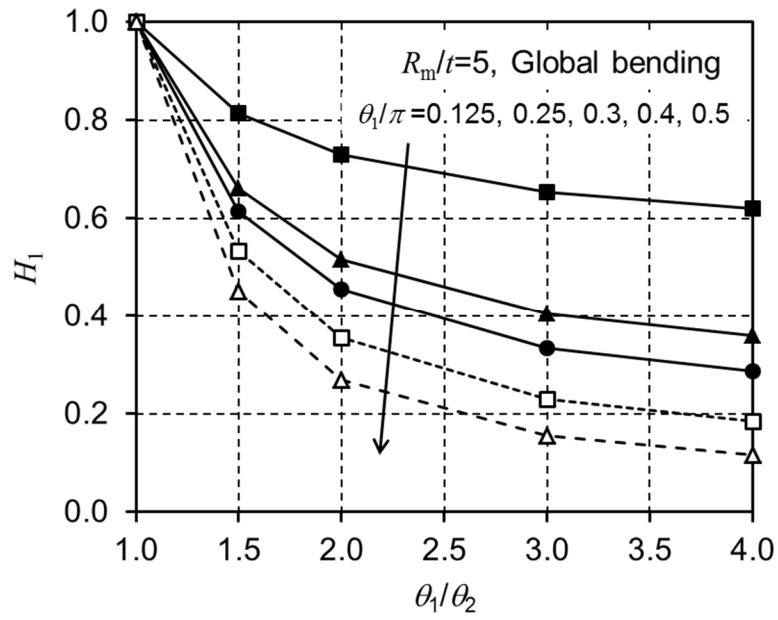
$R_m/t$	$\theta_1/\pi$	$\theta_1/\theta_2$				
		1	1.5	2	3	4
2	0.125	1.000	0.723	0.579	0.427	0.344
	0.25	1.000	0.665	0.509	0.364	0.293
	0.3	1.000	0.633	0.471	0.327	0.261
	0.4	1.000	0.557	0.385	0.249	0.193
	0.5	1.000	0.466	0.292	0.173	0.129
5	0.125	1.000	0.702	0.550	0.399	0.323
	0.25	1.000	0.644	0.471	0.316	0.246
	0.3	1.000	0.613	0.435	0.283	0.216
	0.4	1.000	0.537	0.354	0.213	0.157
	0.5	1.000	0.441	0.264	0.146	0.103
10	0.125	1.000	0.681	0.516	0.358	0.283
	0.25	1.000	0.617	0.435	0.276	0.207
	0.3	1.000	0.585	0.399	0.245	0.180
	0.4	1.000	0.507	0.321	0.184	0.130
	0.5	1.000	0.413	0.238	0.126	0.086
20	0.125	1.000	0.656	0.480	0.317	0.242
	0.25	1.000	0.584	0.395	0.238	0.172
	0.3	1.000	0.551	0.361	0.211	0.149
	0.4	1.000	0.473	0.289	0.158	0.108
	0.5	1.000	0.381	0.212	0.108	0.071

**Table 10.  $H_1$  values for non-idealized circumferential TWC under global bending**

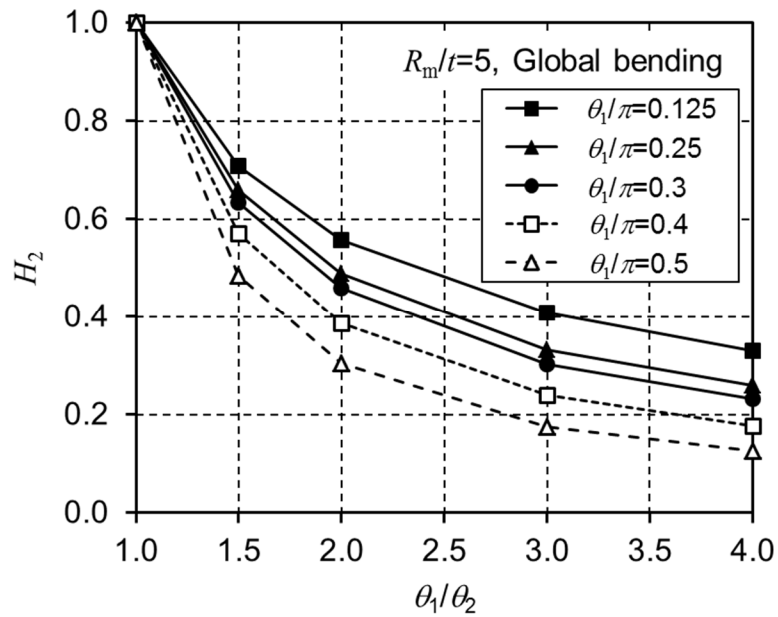
$R_m/t$	$\theta_1/\pi$	$\theta_1/\theta_2$				
		1	1.5	2	3	4
2	0.125	1.000	0.860	0.800	0.746	0.721
	0.25	1.000	0.709	0.593	0.501	0.463
	0.3	1.000	0.658	0.523	0.420	0.380
	0.4	1.000	0.566	0.405	0.291	0.250
	0.5	1.000	0.480	0.307	0.195	0.158
5	0.125	1.000	0.815	0.730	0.654	0.620
	0.25	1.000	0.661	0.517	0.404	0.360
	0.3	1.000	0.615	0.455	0.334	0.288
	0.4	1.000	0.535	0.355	0.230	0.186
	0.5	1.000	0.452	0.270	0.155	0.117
10	0.125	1.000	0.760	0.650	0.557	0.517
	0.25	1.000	0.607	0.439	0.313	0.266
	0.3	1.000	0.569	0.389	0.258	0.210
	0.4	1.000	0.503	0.313	0.182	0.137
	0.5	1.000	0.428	0.244	0.128	0.089
20	0.125	1.000	0.688	0.550	0.440	0.396
	0.25	1.000	0.560	0.373	0.236	0.187
	0.3	1.000	0.532	0.339	0.199	0.150
	0.4	1.000	0.476	0.283	0.149	0.103
	0.5	1.000	0.405	0.225	0.110	0.071

**Table 11.  $H_2$  values for non-idealized circumferential TWC under global bending**

$R_m/t$	$\theta_1/\pi$	$\theta_1/\theta_2$				
		1	1.5	2	3	4
2	0.125	1.000	0.734	0.594	0.443	0.360
	0.25	1.000	0.686	0.534	0.388	0.316
	0.3	1.000	0.660	0.501	0.355	0.286
	0.4	1.000	0.596	0.425	0.284	0.223
	0.5	1.000	0.517	0.339	0.210	0.159
5	0.125	1.000	0.709	0.558	0.408	0.331
	0.25	1.000	0.660	0.489	0.333	0.260
	0.3	1.000	0.635	0.459	0.302	0.233
	0.4	1.000	0.571	0.387	0.240	0.178
	0.5	1.000	0.486	0.304	0.175	0.126
10	0.125	1.000	0.686	0.522	0.363	0.288
	0.25	1.000	0.632	0.450	0.289	0.218
	0.3	1.000	0.605	0.419	0.261	0.193
	0.4	1.000	0.539	0.351	0.205	0.147
	0.5	1.000	0.456	0.275	0.151	0.104
20	0.125	1.000	0.661	0.485	0.321	0.246
	0.25	1.000	0.598	0.409	0.249	0.181
	0.3	1.000	0.570	0.379	0.224	0.160
	0.4	1.000	0.504	0.316	0.176	0.122
	0.5	1.000	0.423	0.246	0.129	0.087



(a)  $H_1$  values



(b)  $H_2$  values

Figure 10. H values for non-idealized circumferential TWCs in pipe ( $R_m/t=5$ ) under global bending

### 2.2.2 Axial Crack

Limited K and COD solutions for non-idealized axial through-wall cracked pipes under internal pressure ( $p$ ) have been published in [6]. In these solutions, the non-idealized axial TWC was characterized by the crack lengths on the ID and OD surfaces ( $2a_1$  and  $2a_2$ , respectively), as shown in Figure 11. Note that K and COD solutions were provided for the crack-tips and the crack center points, respectively. More importantly, the crack front shape was assumed as a straight line for simplicity. Hence, a study was required to investigate if these solutions are applicable for an axial crack transition model.

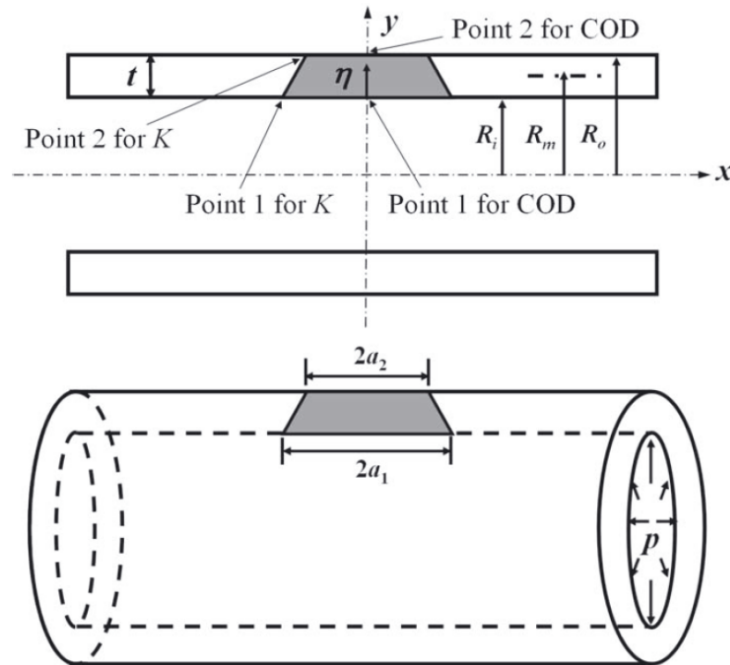


**Figure 11. Shape of non-idealized axial TWC assumed in [6]**

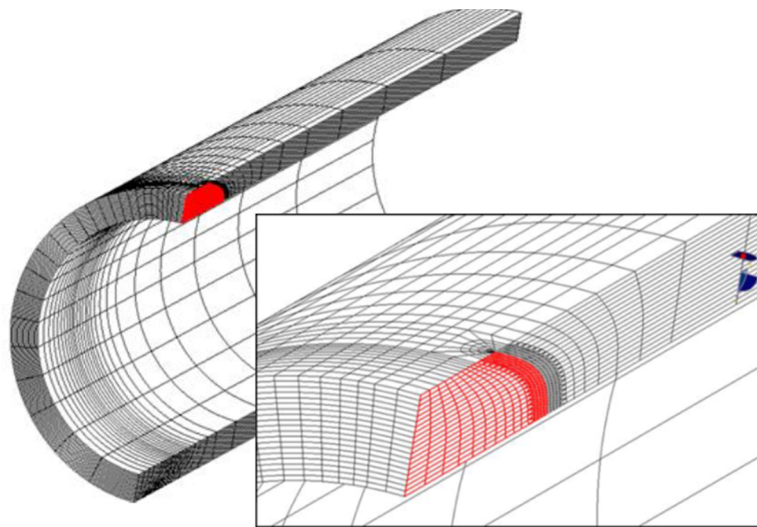
As part of xLPR Ver. 2.0 development, an Advanced Finite Element Analysis (AFEA) study was conducted to define the appropriate crack front shape for non-idealized axial TWCs using natural crack growth simulations. The details of the AFEA calculations are provided in [9] and are not reported here for brevity.

Figure 12 shows an example FE mesh of a non-idealized TWC that was obtained during the natural crack growth analysis. The overall AFEA results are illustrated in Figure 13 where the natural crack shapes obtained during the crack transition are provided. As demonstrated in this figure, after wall penetration, the crack grows very slowly at the ID surface. On the other hand, the crack grows relatively rapidly at the OD surface. Eventually, the OD crack length equals the ID crack length and thus forms a shape that is very close to an idealized TWC.

The natural crack front shape was compared against the straight crack front since the main purpose of conducting the natural crack growth analysis was to investigate the applicability of the existing K and COD solutions where a straight crack front is assumed. Figure 14(a) shows the comparison at wall penetration, i.e., initial TWC. The natural crack front shape has a curvature which is similar to a partial semi-elliptical surface crack front and shows a large deviation from a straight crack front. Figure 14(b) illustrates the effect of crack shape on K values along the crack

front. As shown in this figure, the K value at the OD surface is significantly higher than that at the ID surface for both natural and straight crack front shapes with the K values being higher for the natural crack front. This implies that the K values would be under-predicted if the straight crack front solutions are used.

Based on these findings, it was concluded that a new method should be used to represent the transitioning crack shape. After examining the natural crack shapes in Figure 13, an attempt was made to represent the natural crack front as part of an ellipse that passed through the crack-tip points at the ID and OD surfaces. Figure 15(a) shows the comparison between the natural and partial ellipse crack fronts at the beginning stage of crack transition. As shown, a reasonable agreement exists between these crack shapes. Additional comparison throughout the crack transition is provided in Figure 15(b). From these results, it was concluded that new solutions developed using the partial ellipse crack front shapes would better represent the natural crack transition than the existing solutions for a straight crack front.



**Figure 12. Example FE mesh of non-idealized axial TWC obtained during natural crack growth**

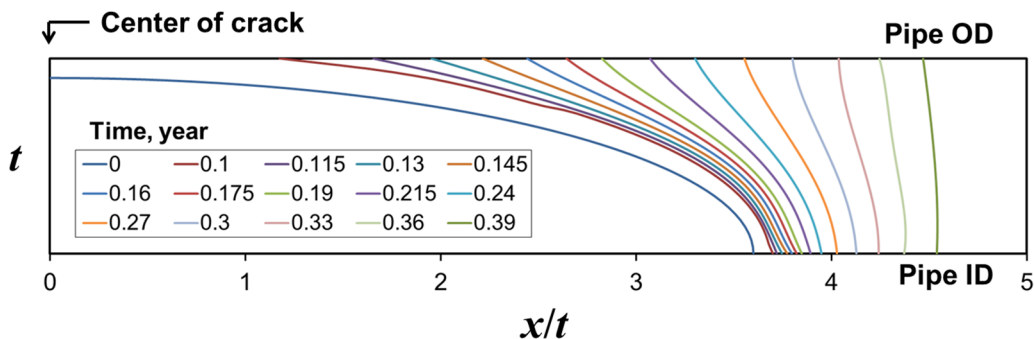
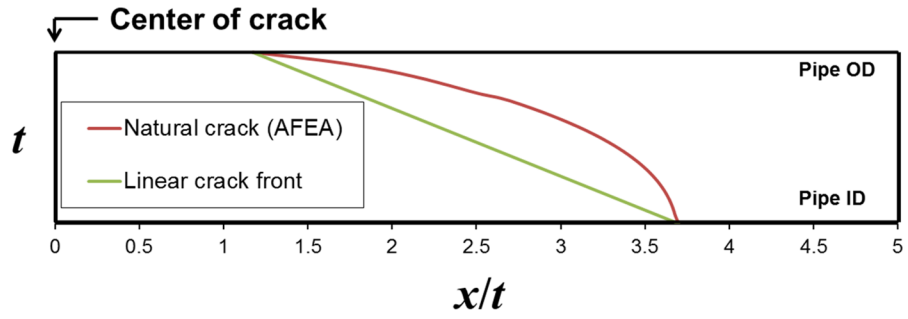
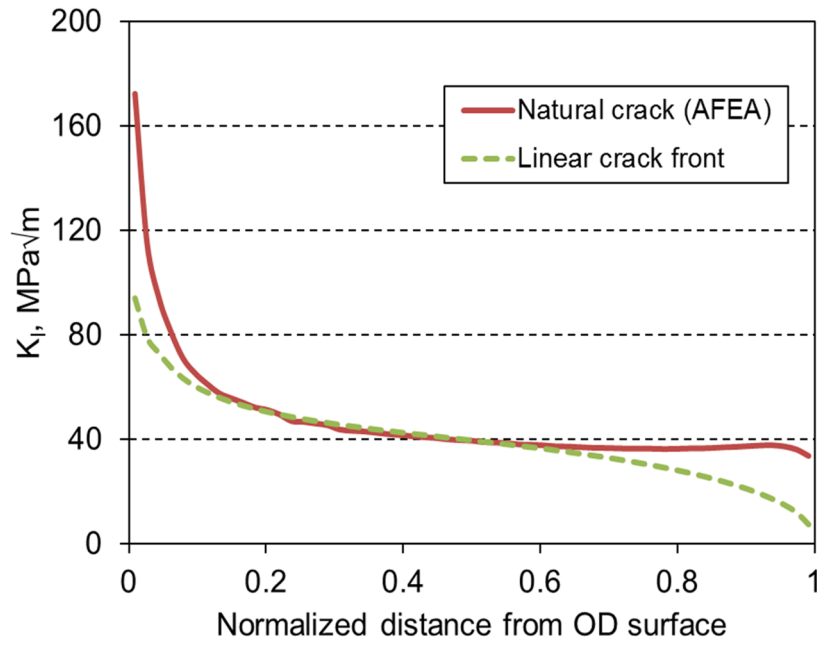


**Figure 13. AFEA results showing the natural crack front shapes obtained during crack transition**

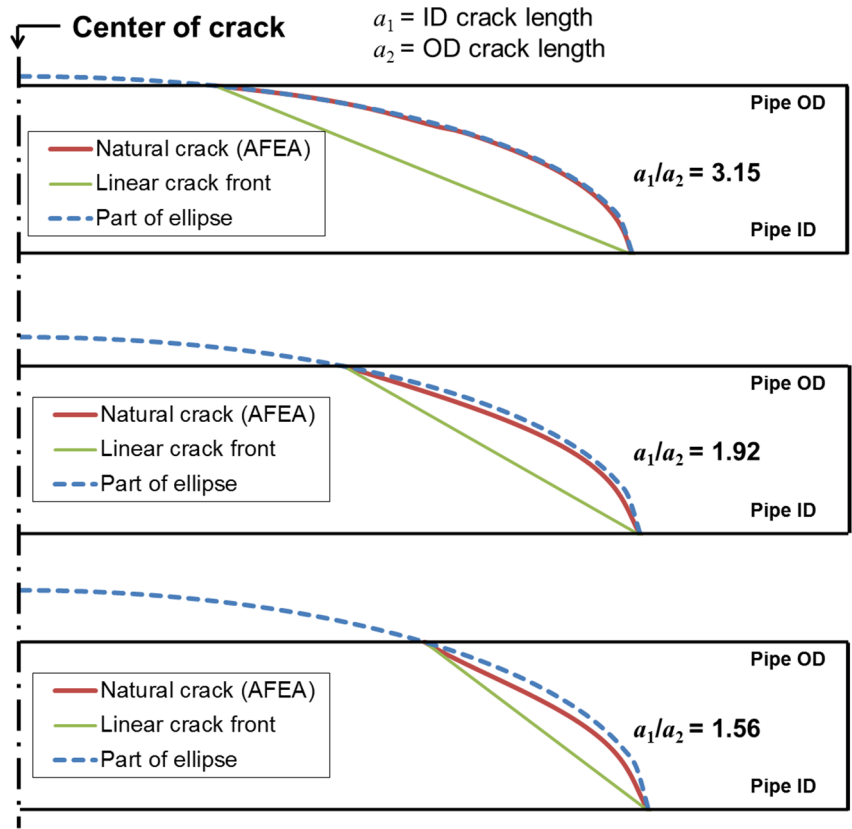


(a)

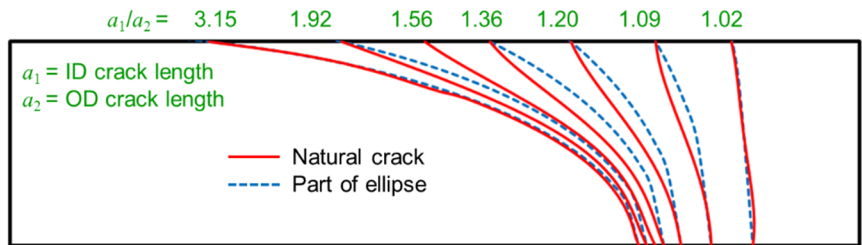


(b)

Figure 14. Comparison of crack front shape (a) and  $K$  values (b) between straight and natural crack



(a)



(b)

**Figure 15. Representation of natural crack front shape using part of an ellipse for (a) crack shapes at early stage of crack transition and (b) for the entire crack transition**

For the new solutions, the relevant dimensions remain the same as in the existing solutions (see Figure 11). The only difference is in the crack front shape. The two half-crack lengths ( $a_1$  and  $a_2$ , where  $a_1 > a_2$ ) are normalized as

$$\rho_1 = \frac{a_1}{\sqrt{R_m t}}, \quad \rho_2 = \frac{a_2}{\sqrt{R_m t}} \quad (\text{Eq. 10})$$

Five different values of  $\rho_1/\rho_2$ , 1, 1.5, 2, 3 and 4, were considered, where  $\rho_1/\rho_2=1$  represents an idealized TWC. Furthermore, four different values of  $R_m/t$  (2, 5, 10, and 20) and four different values of  $\rho_1$  (0.5, 1, 2 and 3) were selected. A total of 80 cases were analyzed.

The FE software, ABAQUS [14] was employed to perform the elastic FE analyses. The material was assumed to be homogeneous, and isotropic linear elastic. The elastic modulus and the Poisson's ratio were set to 190 GPa and 0.3, respectively. Figure 12 shows a typical 3-D FE mesh employed, where a quarter model was used due to symmetric conditions. Twenty-node reduced integration solid elements were used. In addition, the crack-tip was modeled with focused wedge type elements, where the mid-point nodes were moved to the quarter point location. The crack-tip was modeled with six contours to calculate the K values. In order to accurately simulate the stress distribution through the thickness, 180 elements were used through the wall thickness along the crack front. Internal pressure was applied to the inner surface of the cylinder and axial tension (due to internal pressure) was applied to the end of the cylinder. Moreover, 50-percent of the internal pressure was applied to the crack face to simulate the crack face pressure effect.

The K values along the crack front were calculated using the interaction integral method in ABAQUS. The final K values were determined as the average value of 3rd, 4th, and 5th contours. Since K values calculated from FE analyses are known to be inaccurate at the free surface, surface point K values were extrapolated using a sixth order polynomial fit of the K values through the entire crack front. Finally, the COD values were obtained from the FE results as the displacement at the center of the crack on both ID and OD surfaces.

In the same context as the existing solutions [6], the K values for the non-idealized TWC were represented using the idealized TWC solutions along with K correction factors ( $G_1$  and  $G_2$ ).

$$K_{I,ID}^{\text{Non-idealized}} = \sigma\sqrt{\pi a_1} \cdot F \cdot G_1 = K_I^{\text{Idealized}} \cdot G_1 \quad (\text{Eq. 11})$$

$$K_{I,OD}^{\text{Non-idealized}} = \sigma\sqrt{\pi a_1} \cdot F \cdot G_2 = K_I^{\text{Idealized}} \cdot G_2 \quad (\text{Eq. 12})$$

where,

$$\sigma = \frac{pR_i}{2t} \quad (\text{Eq. 13})$$

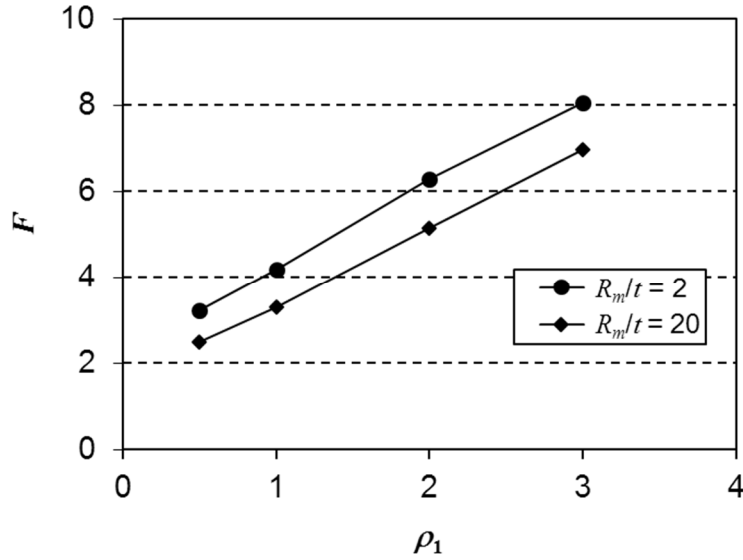
and F denotes the shape function for the idealized TWC ( $a_1 = a_2$  or  $\rho_1 = \rho_2$ ) with a half-crack length of  $a_1 [= \rho_1 \sqrt{(R_m t)}]$ . Similarly, the COD values for the non-idealized TWC can be represented as,

$$\text{COD}_{ID}^{\text{Non-idealized}} = \frac{4\sigma a_1}{E} \cdot V_1 \cdot H_1 = \text{COD}^{\text{Idealized}} \cdot H_1 \quad (\text{Eq. 14})$$

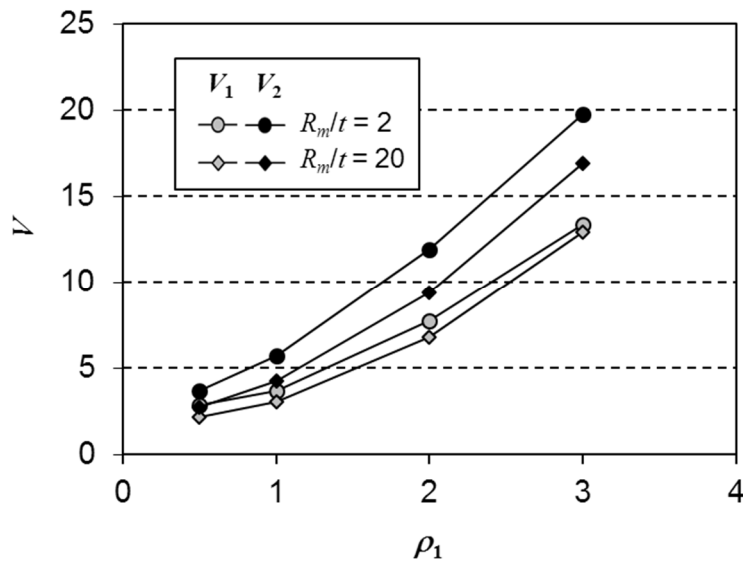
$$\text{COD}_{OD}^{\text{Non-idealized}} = \frac{4\sigma a_1}{E} \cdot V_2 \cdot H_2 = \text{COD}^{\text{Idealized}} \cdot H_2 \quad (\text{Eq. 15})$$

where,  $V_1$  and  $V_2$  are the shape functions for the idealized TWC at the ID and OD surfaces, respectively. Furthermore,  $H_1$  and  $H_2$  are the COD correction factors for the non-idealized TWC.

Figure 16 shows the variation of the shape functions ( $F$ ,  $V_1$ , and  $V_2$ ) for idealized axial TWC under internal pressure for the bounding  $R_m/t$  values. Values for all cases considered in this paper are provided in Table 12. These values show good agreement with those provided in [6] and other past publication [10].



(a)



(b)

**Figure 16. Variation of shape functions (a)  $F$  and (b)  $V_1$  and  $V_2$  for idealized axial TWC under internal pressure**

**Table 12. F, V<sub>1</sub> and V<sub>2</sub> values for idealized axial TWC under internal pressure**

<b>R<sub>m</sub>/t</b>	<b>ρ<sub>1</sub></b>	<b>F</b>	<b>V<sub>1</sub></b>	<b>V<sub>2</sub></b>
2	0.5	3.230	2.855	3.704
	1	4.197	3.706	5.737
	2	6.293	7.724	11.908
	3	8.068	13.390	19.789
5	0.5	2.720	2.360	3.066
	1	3.556	3.222	4.697
	2	5.484	7.108	10.118
	3	7.322	13.182	17.708
10	0.5	2.577	2.237	2.859
	1	3.378	3.094	4.387
	2	5.258	6.909	9.625
	3	7.093	13.026	17.170
20	0.5	2.499	2.184	2.749
	1	3.291	3.038	4.233
	2	5.152	6.818	9.384
	3	6.983	12.937	16.897

The K and COD correction factors determined from the present work are summarized in Table 13 through Table 16. The trends of the K correction factors (G<sub>1</sub> and G<sub>2</sub>) for various reference crack lengths (ρ<sub>1</sub>) and crack ratios (ρ<sub>1</sub>/ρ<sub>2</sub>) for R<sub>m</sub>/t=5 are shown in Figure 17. As illustrated in this figure, the values of the correction factor at the ID surface (G<sub>1</sub>) are less than 1.0, whereas values of the correction factor at the OD surface (G<sub>2</sub>) are greater than 1.0. Similar plots are provided for the COD correction factors (H<sub>1</sub> and H<sub>2</sub>) in Figure 18, where both values are less than 1.0 for all cases. As shown in Figure 17 and Figure 18, the amount of correction needed for the idealized solutions increases as the reference crack length (ρ<sub>1</sub>) increases.

**Table 13.  $G_1$  values for non-idealized axial TWC under internal pressure**

$R_m/t$	$\rho_1$	$\rho_1/\rho_2$				
		1	1.5	2	3	4
2	0.5	1.000	0.941	0.934	0.930	0.923
	1	1.000	0.825	0.784	0.744	0.719
	2	1.000	0.716	0.599	0.491	0.435
	3	1.000	0.591	0.429	0.313	0.269
5	0.5	1.000	0.862	0.858	0.850	0.830
	1	1.000	0.766	0.728	0.663	0.631
	2	1.000	0.658	0.522	0.381	0.313
	3	1.000	0.541	0.357	0.240	0.205
10	0.5	1.000	0.839	0.821	0.802	0.785
	1	1.000	0.749	0.674	0.584	0.532
	2	1.000	0.570	0.415	0.278	0.234
	3	1.000	0.447	0.284	0.203	0.166
20	0.5	1.000	0.820	0.797	0.750	0.728
	1	1.000	0.702	0.595	0.485	0.428
	2	1.000	0.462	0.307	0.227	0.199
	3	1.000	0.358	0.243	0.166	0.121

**Table 14.  $G_2$  values for non-idealized axial TWC under internal pressure**

$R_m/t$	$\rho_1$	$\rho_1/\rho_2$				
		1	1.5	2	3	4
2	0.5	1.000	1.234	1.301	1.257	1.175
	1	1.000	1.730	1.807	1.630	1.473
	2	1.000	2.544	2.440	1.957	1.651
	3	1.000	2.909	2.562	2.014	1.709
5	0.5	1.000	1.490	1.577	1.478	1.360
	1	1.000	2.067	2.052	1.747	1.518
	2	1.000	2.914	2.565	1.793	1.383
	3	1.000	3.040	2.488	1.810	1.440
10	0.5	1.000	1.716	1.760	1.581	1.432
	1	1.000	2.344	2.178	1.743	1.465
	2	1.000	3.093	2.457	1.579	1.220
	3	1.000	2.947	2.393	1.708	1.263
20	0.5	1.000	1.918	1.876	1.624	1.458
	1	1.000	2.509	2.187	1.672	1.396
	2	1.000	3.056	2.217	1.486	1.156
	3	1.000	2.872	2.330	1.490	0.962

**Table 15.  $H_1$  values for non-idealized axial TWC under internal pressure**

$R_m/t$	$\rho_1$	$\rho_1/\rho_2$				
		1	1.5	2	3	4
2	0.5	1.000	0.954	0.937	0.924	0.920
	1	1.000	0.854	0.789	0.738	0.719
	2	1.000	0.712	0.563	0.446	0.403
	3	1.000	0.645	0.454	0.308	0.256
5	0.5	1.000	0.950	0.931	0.917	0.912
	1	1.000	0.846	0.776	0.721	0.702
	2	1.000	0.689	0.536	0.422	0.382
	3	1.000	0.614	0.421	0.283	0.237
10	0.5	1.000	0.946	0.923	0.907	0.902
	1	1.000	0.838	0.763	0.705	0.684
	2	1.000	0.669	0.514	0.403	0.365
	3	1.000	0.591	0.400	0.267	0.223
20	0.5	1.000	0.941	0.914	0.894	0.888
	1	1.000	0.827	0.747	0.686	0.665
	2	1.000	0.649	0.494	0.384	0.348
	3	1.000	0.571	0.381	0.252	0.210

**Table 16.  $H_2$  values for non-idealized axial TWC under internal pressure**

$R_m/t$	$\rho_1$	$\rho_1/\rho_2$				
		1	1.5	2	3	4
2	0.5	1.000	0.751	0.626	0.498	0.431
	1	1.000	0.725	0.585	0.451	0.387
	2	1.000	0.668	0.487	0.332	0.267
	3	1.000	0.632	0.427	0.261	0.197
5	0.5	1.000	0.753	0.629	0.504	0.441
	1	1.000	0.698	0.547	0.410	0.349
	2	1.000	0.624	0.435	0.282	0.222
	3	1.000	0.588	0.378	0.218	0.159
10	0.5	1.000	0.744	0.615	0.489	0.427
	1	1.000	0.676	0.517	0.378	0.317
	2	1.000	0.595	0.403	0.253	0.195
	3	1.000	0.558	0.348	0.194	0.139
20	0.5	1.000	0.730	0.593	0.463	0.401
	1	1.000	0.655	0.490	0.349	0.287
	2	1.000	0.571	0.378	0.231	0.175
	3	1.000	0.535	0.326	0.176	0.122

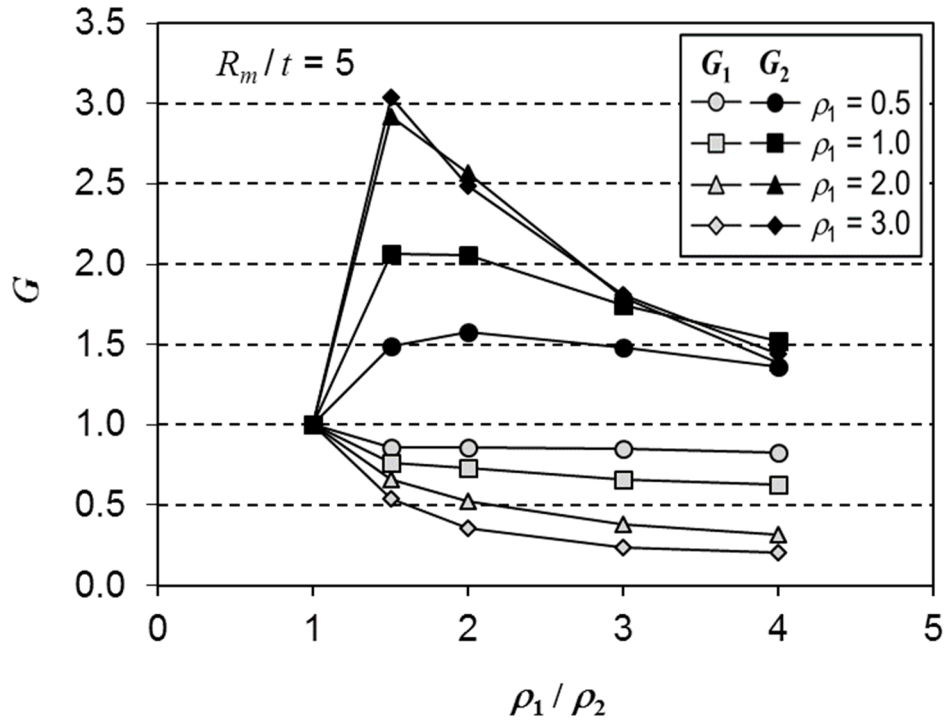
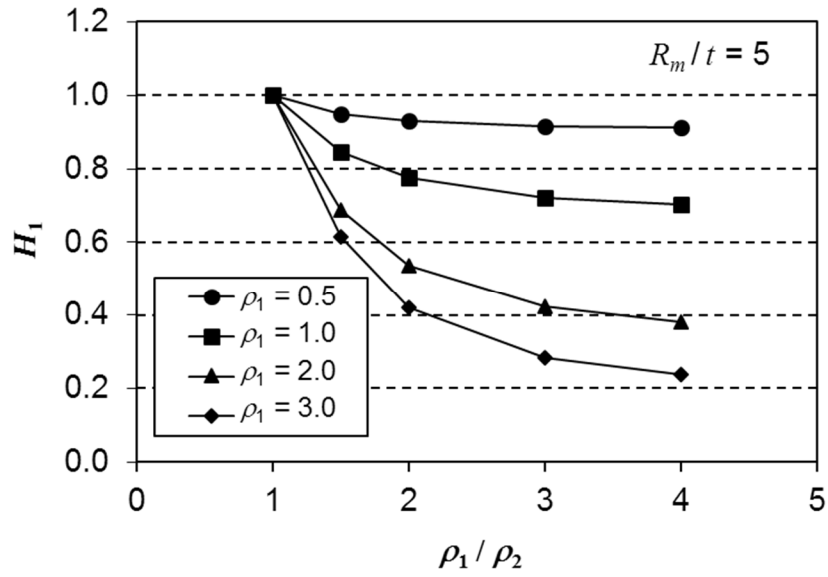
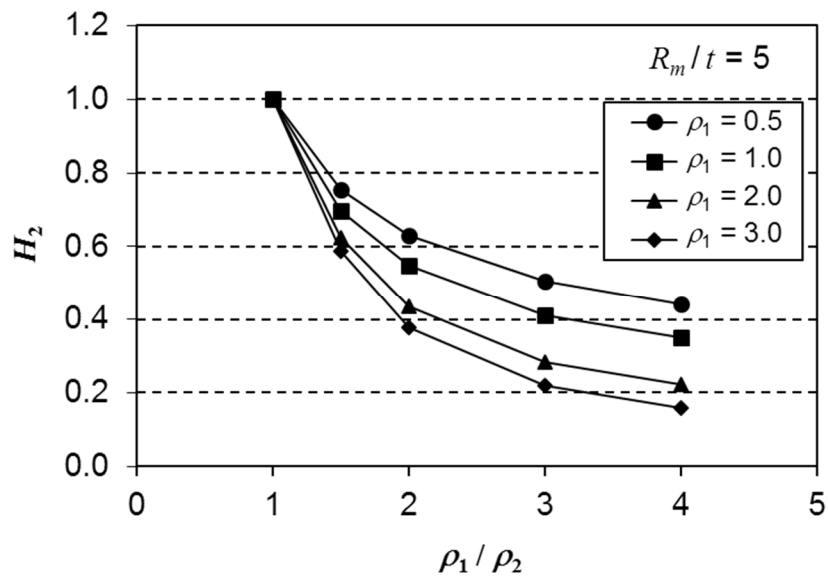


Figure 17. Variation of correction factors ( $G_1$  and  $G_2$ ) for non-idealized axial TWC under internal pressure ( $R_m/t=5$ )



(a)



(b)

Figure 18. Variation of correction factors (a)  $H_1$  and (b)  $H_2$  for non-idealized axial TWC under internal pressure ( $R_m/t=5$ )

## 2.3 Crack Transition Model

The CT model transitions a sub-critical surface crack to an initial non-idealized TWC. Note that this model assumes that there is no ductile tearing or local ligament collapse. Once the initial non-idealized TWC has been defined, the K and COD solutions for the non-idealized TWC are used to calculate the continued crack growth rate and the leak rate until the crack becomes an idealized TWC. A step-by-step procedure is provided below for a circumferential crack case.

### Step 1 – Final surface crack to initial non-idealized TWC

A criterion for transitioning the subcritical surface crack to the initial non-idealized TWC has been developed based on the guidance provided in R6<sup>a</sup> [15]. In this criterion, the crack transition occurs once the surface crack depth reaches 95% of the wall thickness. Furthermore, the two crack lengths (at ID and OD surfaces) of the initial non-idealized TWC are determined as shown in Figure 19. As depicted in this figure, the ID crack length ( $c_1^*$ ) remains identical to the final surface crack length ( $c_1$ ). The OD crack length ( $c_2^*$ ) is determined as either the pipe thickness ( $t$ ) or  $1/4$  of the final surface crack length ( $c_1/4$ ), whichever is less. Once the ID and OD crack lengths have been determined, the crack front shape will be assumed to be the same as was used for the development of non-idealized TWC K and COD solutions, i.e., the curvature due to cylindrical transformation.

### Step 2 – Calculation of K and COD values

Once the ID and OD crack lengths (or angles) of the non-idealized TWC have been determined, the K and COD values at the ID and OD surfaces can be calculated using the non-idealized K and COD solutions described in the previous section. First, the K value for the idealized TWC with the same length (or angle) on the ID surface (dashed line in Figure 20),  $K_{\text{idealized}}$  is calculated. Then, the correction factors ( $G_1$  and  $G_2$ ), which are functions of  $R_m/t$ ,  $\theta_1/\pi$ ,  $\theta_1/\theta_2$ , and loading type, are calculated for the ID and OD points of the non-idealized TWC. Linear interpolation of the tabulated correction factors is used for values not given in the tables. Since the G values are provided for single loading conditions, the applied load (or stress) is decomposed into global bending and axial tension. For each loading condition, non-idealized K values are calculated at the ID and OD surfaces using the correction factors. The total K value is obtained through superposition of the K values from each loading. Using a similar method, the COD values are calculated for the non-idealized TWC.

### Step 3 – Crack growth calculation

Once the K values are calculated for both the ID and OD surface points of the non-idealized TWC, the crack is grown at the ID and OD points according to the K-based crack growth rate to obtain the next non-idealized TWC as shown in Figure 21. Now, a new set of  $\theta_1/\pi$  and  $\theta_1/\theta_2$  values are obtained. For this new non-idealized TWC, K values are calculated using the method described in the previous step. This process is repeated until  $\theta_1/\theta_2=1.05^b$ , where the K model for an idealized TWC can be applied with no further correction.

Similar steps are applied for the axial crack in the CT model and are not provided here for brevity.

---

<sup>a</sup> The guidance provided in R6 was developed from experimental results where the load levels were sufficiently low to prevent significant ductile tearing.

<sup>b</sup> This criterion was determined from observations made from the natural crack growth results, where the TWC maintained this ratio (on average) as it grew around the circumference (see [2] for examples).

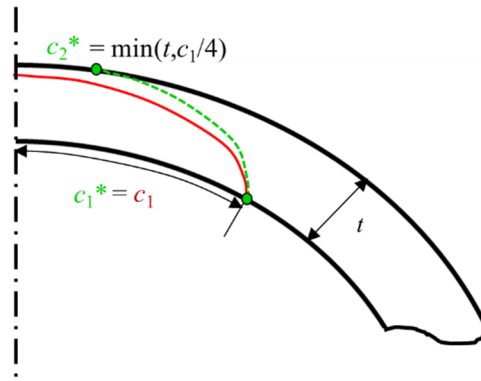


Figure 19. Illustration of crack transition from SC to initial non-idealized TWC

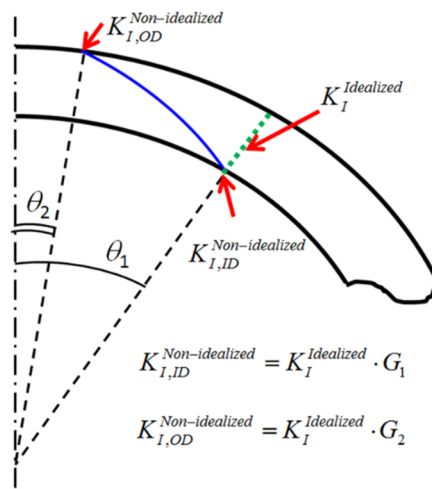


Figure 20. Idealized TWC (dashed line) used for calculation of K and COD for non-idealized TWC

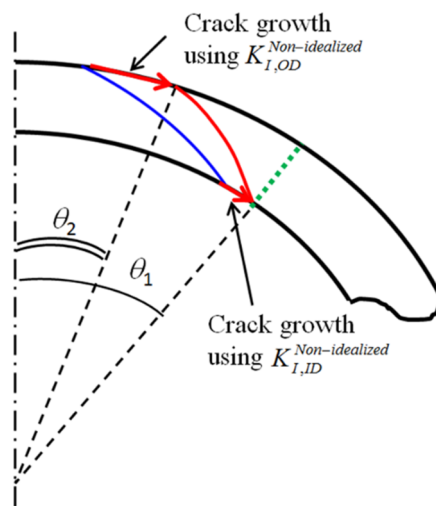


Figure 21. Crack growth calculation using K values at ID and OD surface points of non-idealized TWC

### 3. MODULE DEVELOPMENT

#### 3.1 Module Requirements

The key requirements for the CT Module are described in the Software Requirements Documents (SRD) [16]. Table 17 lists the requirements specified in the SRD. Those requirements appended with an asterisk at the end (i.e., RTC-16\* thru RTC-23\*) are Framework interface or integration requirements. These requirements relate to the interfacing of the CT Module with the overhead DLL wrapper, the xLPR Computational Framework, or other Models Group modules, such as the Crack Growth or Leak Rate modules.

In addition, the CT Module uses the following interfaces:

- It receives information on pipe geometry, crack geometry, and applied loads as defined/calculated by the Computational Framework
- It outputs K and COD correction factors at the inner diameter and outer diameter locations to the Framework for subsequent use in crack growth and leak rate calculations.
- The Framework performs actions based on warning flags provided by the module
  - Warnings should be logged for user interpretation.

Figure 22 shows the flow diagram of the CT Module. Flow elements outside the CT Module boxes represent Framework details that are required to use the output from this module.

**Table 17. SRD requirements for crack transition model**

<b>Requirement</b>	<b>Short Description of Requirements</b>
RTC-1	Separate correction factors are required to modify the idealized K and COD for a transitioning crack
RTC-2	Separate correction factors are also required for axially and circumferentially orientated cracks
RTC-3	Figure 1 of the SRD provides a schematic describing the Crack Transition Module (CTM)
RTC-4	The K correction factors as described in [8] and [9] of this report shall be used
RTC-5	Extrapolation of the correction factors beyond their limits shall not be allowed since no study has been performed to demonstrate the applicability of the extrapolated solutions
RTC-6	If the inputs violate the limits shown in Table 1 of SRD, a warning message should be output
RTC-7	The K correction factors calculated in this subroutine shall be passed to the Framework
RTC-8	Input and output variables described in Tables 2 and 3 of the SRD shall be used for the Ktransition subroutine
RTC-9	The COD correction factors as described in [8] and [9] of this report shall be used

Requirement	Short Description of Requirements
RTC-10	Extrapolation of the correction factors beyond their limits shall not be allowed since no study has been performed to demonstrate the applicability of the extrapolated solutions
RTC-11	If the inputs violate the limits shown in Table 4 of the SRD, a warning message should be output
RTC-12	The COD correction factors calculated in this subroutine shall be passed to the Framework
RTC-13	Input and output variables described in Tables 4 and 5 of the SRD shall be used for the CODtransition subroutine
RTC-14	The Module must be developed so that the resulting DLL to be integrated into the GoldSim Probabilistic SW Program can be replaced easily by another similar functioning DLL module
RTC-15	The module coding will follow the xLPR coding guidelines
RTC-16*	The Framework shall call the Crack Transition module when any of the following conditions are met Any active surface crack where $A/t \geq 0.95$ Any transitioning crack where $\theta_1/\theta_2$ or $a_1/a_2 > 1.05$
RTC-17*	The Framework shall calculate the initial OD and ID crack length Circumferential crack - $\theta_1 = \theta = c/R_i$ Circumferential crack - $\theta_2 = \min(t/R_o, \theta/4)$ Axial crack - $a_1 = a$ Axial crack - $a_2 = \min(t, a/4)$
RTC-18*	If the module is called from the DLL wrapper, communication of inputs and outputs shall be conducted with explicit passing of variables.
RTC-19*	The Framework shall call the Crack Transition subroutines with a set of inputs that are in conformance with the required units, range of validity and data types, specified in Tables 2 and 4 of the SRD
RTC-20*	The Framework shall also accept the outputs in conformance with the required units, range of validity and data types, specified in Tables 3 and 5 of the SRD
RTC-21*	The Framework shall perform specified calculations at the current time step after module is called
RTC-22*	The Framework shall perform specified calculations at the next time step after module is called
RTC-23*	Upon receiving error codes from this module (summarized in Table 6 of the SRD), the Framework shall note the error, but continue the calculations uninterrupted.
RTC-24	The User Manual shall contain minimum requirements

\* Framework requirement

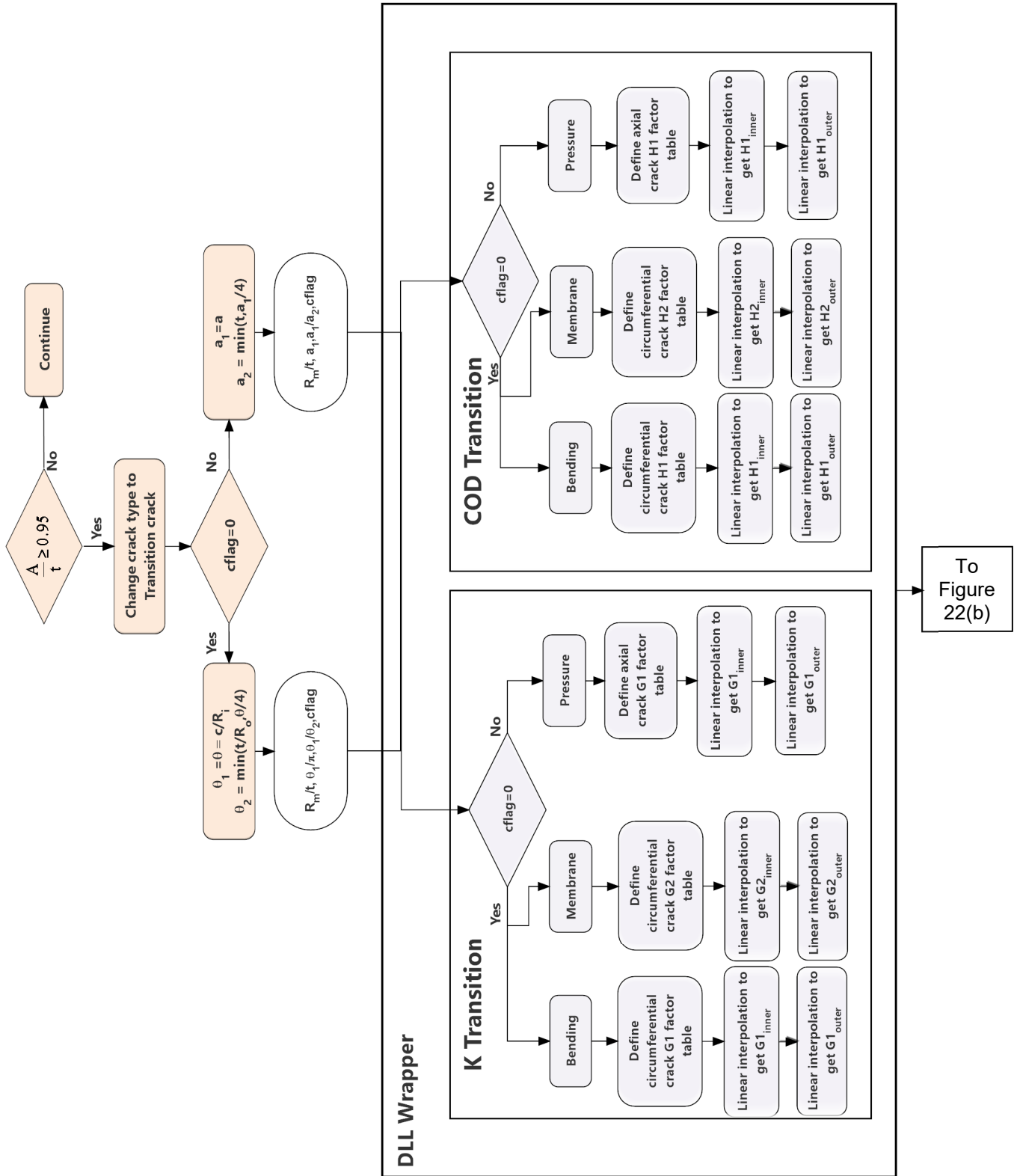


Figure 22. (a) Flow Diagram of the Version 2.0 xLPR Crack Transition Module

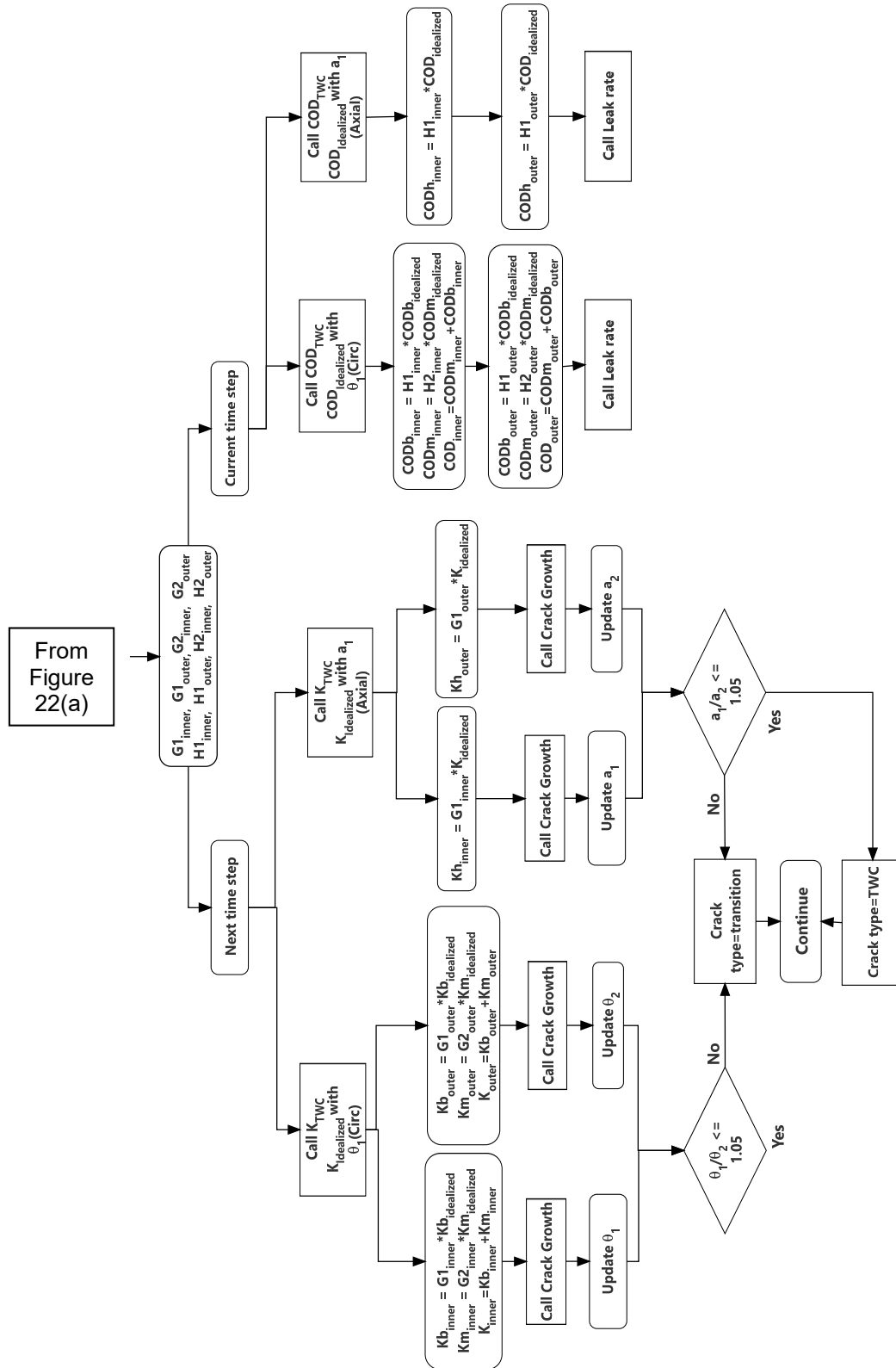


Figure 22. (b) Flow diagram showing details of how the Framework uses the output from CT Module

### 3.2 Module Inputs and Outputs

The specific input and output variables used by the CT Module are described in Table 18 and Table 19, respectively. Table 20 specifies a list of warnings (a log of the warning should be maintained for subsequent user interpretation).

**Table 18. CT Module input parameters**

Input Variable	Description	Units	Type	Limits / Comments
Rm	Pipe mean radius	m	Real (8)	$2 \leq Rm/t \leq 20$
T	Pipe wall thickness	m	Real (8)	$2 \leq Rm/t \leq 20$
CLID	ID Crack angle ( $\theta_1$ ) – Circ Crack ID Crack length ( $a_1$ ) – Axial crack	Rad. m	Real (8)	$< \pi$ – Circ crack $< 25t$ – Axial crack
CLOD	OD crack angle ( $\theta_2$ )– Circ Crack OD crack length ( $a_2$ ) – Axial crack	Rad. m	Real (8)	$< \pi$ – Circ crack $< 25t$ – Axial crack
cflag	Circumferential / axial crack flag	None	Integer	Cflag=0 – Circ crack Cflag=1 – Axial Crack

**Table 19. CT Module output parameters**

Output Variable	Description	Units	Type	Limits / Comments
G1i	Correction factor for ID	None	Real (8)	G1=Gbending for cflag=0 G1=Ghoop for cflag=1
G1o	Correction factor for OD	None	Real (8)	G1=Gbending for cflag=0 G1=Ghoop for cflag=1
G2i	Correction factor for ID	None	Real (8)	G2 = Gtension for cflag=0 G2=0 for cflag=1
G2o	Correction factor for OD	None	Real (8)	G2 = Gtension for cflag=0 G2=0 for cflag=1
H1i	Correction factor for ID	None	Real (8)	H1=Gbending for cflag=0 H1=Ghoop for cflag=1
H1o	Correction factor for OD	None	Real (8)	H1=Gbending for cflag=0 H1=Ghoop for cflag=1
H2i	Correction factor for ID	None	Real (8)	H2 = Htension for cflag=0 H2=0 for cflag=1
H2o	Correction factor for OD	None	Real (8)	H2 = Gtension for cflag=0 H2=0 for cflag=1
IError	Error code	None	Integer	See Table 20

**Table 20. Error and warning flags used in the CT Module**

<b>Error Code</b>	<b>Description</b>	<b>Module Guidance to Framework</b>
301	$R_m/t$ is less than 2 or greater than 20	Bounds of solution have been reached. $R_m/t=2$ and $R_m/t=20$ solutions will be used for $R_m/t<2$ and $R_m/t>20$ , respectively.
302	CLID_over_CLOD is greater than 4	Bounds of solution have been reached. CLID_over_CLOD=4 solutions will be used for CLID_over_CLOD>4.
303	CLID_over_pi is less than 0.125 or greater than 0.5 for circumferential transitioning crack	Bounds of solution have been reached. CLID_over_pi=0.125 and CLID_over_pi=0.5 solutions will be used for CLID_over_pi<0.125 and CLID_over_pi>0.5, respectively.
304	CLID_over_√(R <sub>m</sub> t) is less than 0.5 or greater than 3 for axial transitioning crack	Bounds of solution have been reached. CLID_over_√(R <sub>m</sub> t)=0.5 and CLID_over_√(R <sub>m</sub> t)=3 solutions will be used for CLID_over_√(R <sub>m</sub> t)<0.5 and CLID_over_√(R <sub>m</sub> t)>3, respectively.

Based on the CT model described in Section 2 of this report, the correction factors are applicable within the range limits summarized in Table 21. In order to calculate the appropriate correction factor, linear interpolation of the correction factor tables is permitted. Extrapolation of the correction factor beyond the limits used in developing the crack size and loading dependent factors is not allowed since no study has been performed to demonstrate the applicability of the extrapolated solutions. The detailed design description of the CT Module is provided in [17].

**Table 21. Range limits for correction factors**

<b>Parameter</b>	<b>Crack type</b>	<b>Valid range</b>
$R_m/t$	Circumferential and Axial	$2 \leq R_m/t \leq 20$
$\theta_1/\theta_2$	Circumferential	$1 \leq \theta_1/\theta_2 \leq 4$
$\theta_1/\pi$	Circumferential	$0.125 \leq \theta_1/\pi \leq 0.5$
$a_1/a_2$	Axial	$1 \leq a_1/a_2 \leq 4$
$a_1/\sqrt{(R_m t)}$	Axial	$0.5 \leq a_1/\sqrt{(R_m t)} \leq 3$

### **3.3 Module Verification and Validation**

This section summarizes the results from the Verification and Validation (V&V) exercises carried out on the CT Module. Further details of the V&V activities can be found in the Software Test Plans (STP) [18], Software Test Results Reports (STRR) [19], and Module Validation Reports (MVR) [20] for the CT Module.

#### **3.3.1 CT Module Verification**

The verification of the CT Module is documented in detail in the STRR for the CT Module [19]. The testing activity described in the STRR was intended to verify that the requirements specified in the CT SRD were met [16]. The STRR covers 15 static test cases and 36 dynamic test cases defined in the CT STP [18]. Some of the requirements in the CT SRD [16] are applicable to the Framework and thus, verification of those requirements has been deferred until integration of the CT Module into the xLPR Framework.

The results from the independent verification of the CT Module, as documented in the STRR [19] are summarized next:

**Manual inspection of source code for requirements – TCTM-S-1 to TCTM-S-15:** Manual inspection of the source code [21] was performed for the requirements in the SRD [16] and SDD [17] in which the verification of design and source code logic is required as part of the acceptance criteria. Test outcomes are reported in Table 3-1 of CT STRR [19]. A JIRA issue XLPR-429 (“Combine FORTRAN files”) was created for the recommendation to combine the various subroutines (in different FORTRAN code files). All of the subroutines for the Crack Transition Module have been combined into one f90 code (“CTM.f90”).

**Manual inspection of code for recommended programming practices – TCTM-S-1 to TCTM-S-15:** Manual inspection of the various subroutines in the source code [21] that form the CT Module was performed against the recommended programming practices [22]. No issues were identified during compilation of the CT Module code or execution of the generated executable file.

**Dynamic test cases for requirements – TCTM-D-1 to TCTM-D-36:** An alternative calculation, in the form of an Excel spreadsheet, was developed to calculate the interpolated correction factors for both the K and COD associated with the circumferential and axial cracks for all the dynamic cases. A FORTRAN driver code was written to execute the dynamic test cases and record the CT Module output. The STP [18] describes specific acceptance criteria for each test case. The test cases required obtaining and recording the code output values for various correction factors for K and COD. For comparison the values obtained from the alternative calculation using Microsoft Excel were found to match for the first three digits past the decimal point. For each dynamic test case, the relevant test outcomes (i.e. verification that the acceptance criteria are met) are reported in Table 3-1 of CT STRR [19]. No anomalies were found since the values calculated using the CT Module code and using Excel spreadsheet were in good agreement.

### 3.3.2 CT Module Validation

#### Description of Validation

The validation of the CT Module is documented in detail in the MVR for the K solution and CT Modules [20]. Since the K parameter cannot be physically measured, it was decided to validate the K solution and CT Modules by employing them in a crack growth calculations (e.g., fatigue or stress corrosion cracking) to compare predicted crack shape evolution with observed crack shape evolution. Since crack growth data (including crack shape evolution data) from operating plants are scarce, a laboratory data set of fatigue crack growth of circumferential cracks in pipes under bending was used for the validation. Validation of the COD correction factors were not carried out since no experimental data was available.

The experimental data used for the present validation was developed by Yoo et al. [3,23] where fatigue crack growth in circumferentially cracked pipes was investigated. In these experiments, a series of surface cracked pipes was loaded under cyclic bending until the surface crack penetrated the pipe wall and transitioned to an idealized through-wall crack. This data is sufficiently representative of field behavior for pipes under cyclic bending.

The pipe material tested in [3] and [23] was a carbon steel (STS370) where the yield and ultimate strengths were 227 MPa and 406 MPa, respectively. The pipe geometry, initial surface crack size, loading condition, and fatigue life (number of cycles to leak and fracture) are summarized in Table 22. The two  $R_m/t$  values of the pipes tested are 5.8 and 3.52 which are close to the pipe sizes of interest in xLPR. The K and CTM modules in xLPR Ver. 2.0 can handle  $R_m/t$  values from 2 to 20.

**Table 22. Pipe geometry, initial surface crack size, loading condition, and fatigue life from experiments conducted by Yoo et al.**

Test ID	Pipe geometry		Initial surface crack size				Loading condition		Fatigue life	
	No.	$R_o$ (mm)	t (mm)	a (mm)	$c_i$ (mm)	a/t -	a/ $c_i$ -	$\sigma_{max}$ (MPa)	$\sigma_{min}$ (MPa)	$N_L^*$ (cycle)
TB-1	51.0	8.1	4.5	22.25	0.556	0.202	200.0	20.0	12,407	21,558
TB-2	51.0	8.1	3.0	6.0	0.370	0.500	210.0	21.0	169,750	197,856
TB-3	51.0	8.1	5.0	5.0	0.618	1.000	325.0	32.5	11,200	17,500
TB-4	51.0	8.1	3.0	18.25	0.370	0.164	200.0	20.0	72,910	862,60
TB-5	51.0	12.7	6.0	6.0	0.236	1.000	220.0	22.2	222,920	245,800
TB-6	51.0	12.7	3.0	6.0	0.236	0.500	261.0	26.1	287,500	301,400

\*  $N_L$ , number of cycles to leak (crack incubation time prior to crack initiation not included)

\*\*  $N_F$ , number of cycles to fracture (definition of fracture is not clearly defined in Ref. [9])

The initial surface crack was produced using electric discharge machining or a saw cut. Fatigue tests were conducted using a four-point bending fixture with outer and inner spans of 1,000 mm and 245 mm, respectively. Fatigue load was applied using a sine wave loading with a stress ratio  $R=0.1$  at a frequency of 1~5 Hz. All tests were conducted at room temperature. In addition, crack growth measurements were made using a stereomicroscope to track beach mark evolution. Example photographs of fatigue fracture surfaces obtained from the experiments are provided in Figure 23. As shown in this figure, the initial surface crack propagated through the pipe wall and

then transitioned into a through-wall crack, which had a shape close to an idealized through-wall crack. Additional details of the fatigue pipe test procedure can be found in [3] and [23].

In [3], the fatigue crack growth rate (FCGR) was determined from the pipe tests. Figure 24 shows the FCGR versus the SIF range ( $\Delta K$ ) from Ref. [3] for samples loaded below the yield strength [Figure 24(a)] and those loaded above the yield strength [Figure 24(b)]. This figure includes the crack growth data measured at the deepest and surface points of the surface crack, and inner and outer surface points of the through-wall crack. The K-solutions used for these figures are provided in [3], where the Newman-Raju solution (for surface cracked plate) [24] was used for surface cracks and Zahoor solution (for through-wall cracked pipe) [10] was used for idealized through-wall cracks. In addition, Yoo et al. [3] developed a simplified K-solution for non-idealized through-wall cracks by modifying the Zahoor solution. However, due to modeling the pipe geometry as a plate, the accuracy of the K-solutions used for the FCGR determinations in Figure 24 may have some uncertainty embedded in it. The effect of this uncertainty on fatigue life predictions is discussed later in this report.

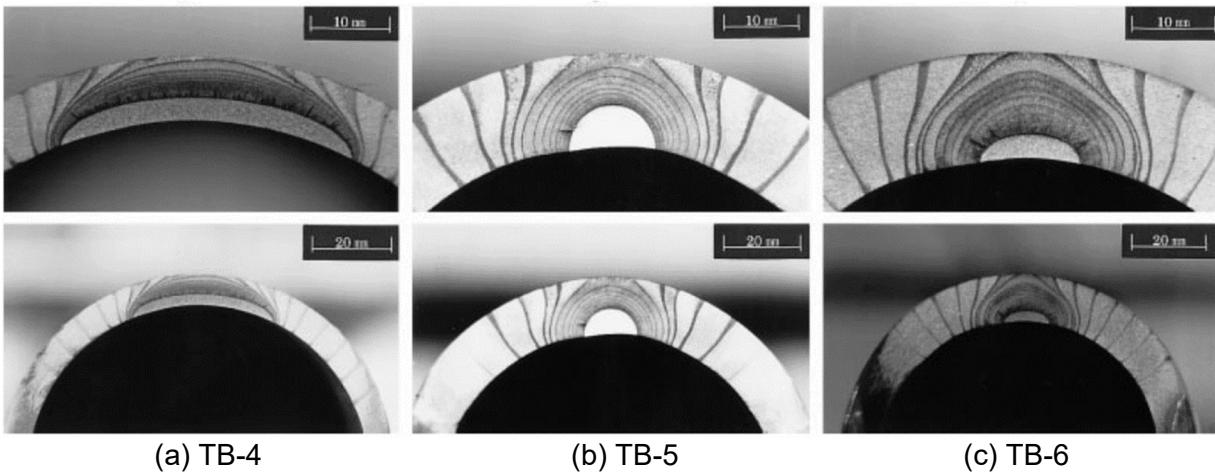
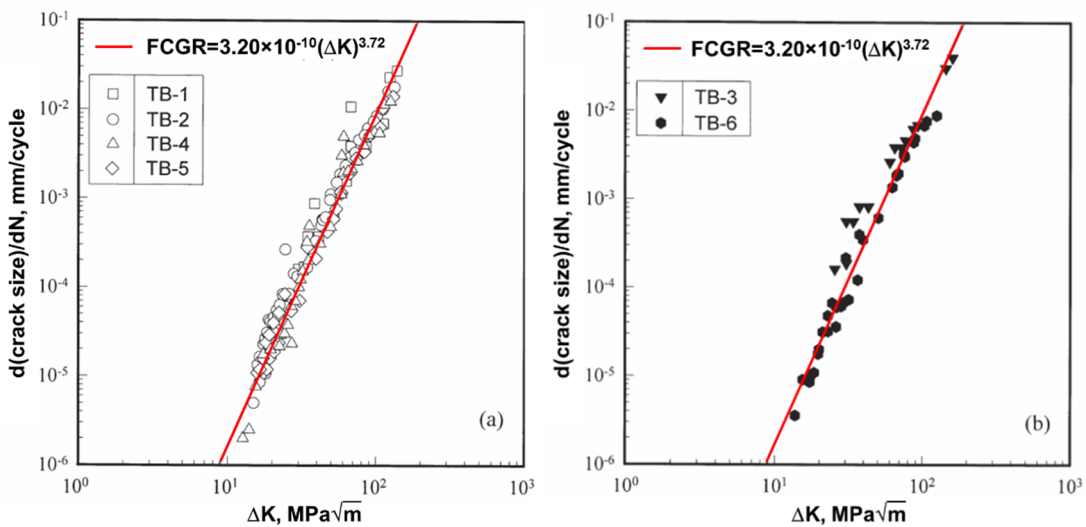


**Figure 23. Example of fatigue fracture surfaces from Ref. [3]**



(a) Cases loaded below yield strength      (b) Cases loaded above yield strength

**Figure 24. Fatigue crack growth rate versus SIF range from Ref. [3]**

The fatigue crack growth results reported in [3] were predicted using the modules in xLPR Version 2.0. These modules include the part- and through-wall K-calculation modules KPW [25], KTW [26] respectively, and CT Modules. The K-solutions in KPW assume that the shape of the surface crack is semi-elliptical. Once the depth of the surface crack reaches 95% of the wall thickness ( $a/t=0.95$ ), the CTM initiates the surface to through-wall crack transition and forms a through-wall crack. This initial non-idealized through-wall crack has different initial crack lengths on the ID and OD surfaces, which are determined by the CT Module. The K values calculated by the CT Module (using correction factors) were used to grow the non-idealized through-wall crack until an idealized through-wall crack is approximated (i.e.,  $\theta_1/\theta_2=1.05$ ). At this point, the CT Module is no longer called and crack growth calculations are continued using idealized through-wall crack K-solutions in KTW. In the present validation, the FCGR parameters reported in [3] were employed as shown in Equation 16 – also see Figure 24.

$$FCGR = da/dN = C(\Delta K)^n = 3.20 \times 10^{-10} (\Delta K)^{3.72} \text{ [mm/cycle]} \quad (\text{Eq. 16})$$

After performing a sensitivity study, the step increment used in the crack growth calculations was fixed to 100 cycles/increment. Note that the crack growth calculations did not include the time to crack initiation, i.e., initial flaw incubation time prior to start of crack growth.

### **Validation Criteria**

The validation parameter for surface cracks was determined as the difference between the experimentally measured and predicted  $a/c$  values at wall penetration ( $a/t=0.95$ ). The acceptance criterion for surface crack was specified as follows.

$$[a/c_{Exp.} - a/c_{Pred.}] / [a/c_{Exp.}] < 0.1 \text{ (at wall penetration, } a/t=0.95) \quad (\text{Eq. 17})$$

For through-wall cracks, crack angles at the ID and OD surfaces were compared. The validation parameter was selected as the difference between the experimentally measured and predicted  $\theta_1/\theta_2$  values at a given  $\theta_2/\pi$  value during the through-wall crack growth. The acceptance criterion for through-wall cracks was specified as follows.

$$[\theta_1/\theta_{2,Exp.} - \theta_1/\theta_{2,Pred.}] / [\theta_1/\theta_{2,Exp.}] < 0.1 \text{ (during through-wall crack growth)} \quad (\text{Eq. 18})$$

Note that both surface and through-wall crack validation criteria are based on crack size/shape. The number of fatigue loading cycles to wall penetration was not considered as the validation parameter due to the uncertainty in the FCGR and the time to crack initiation.

### **Validation Results**

In order to validate the surface crack K-solutions, predictions from the K modules were compared against the surface crack growth results obtained from the experiments. The validation of surface crack K-solutions is included in this report since the K-solution and CT Modules were validated together using the same set of experimental data. Figure 25 provides the change in crack depth ( $a/t$ ) as well as crack aspect ratio ( $a/c$ ) during surface crack growth. The predicted results are provided up to  $a/t=0.95$ , when the surface crack is transitioned to a through-wall crack according to the CT model. As demonstrated in Figure 25, overall results show good agreement between the predicted and experimental results. The agreement is excellent for cases where the initial crack aspect ratio ( $a/c$ ) is relatively low, i.e., long surface cracks – TB-1 and TB-4. This indicates that, for these cases, the surface crack maintains a semi-elliptical shape during the crack growth [see Figure 23(a)]. Hence, the crack shape evolution is accurately predicted by the surface crack

K-solutions. On the other hand, for initial surface cracks with  $a/c=0.5$  (TB-2 and TB-6), the two results showed good agreement in the earlier stage of crack growth but then deviated from each other as the crack depth increased. This is due to the surface crack shape deviating from the semi-elliptical shape in the experiment – especially as it gets closer to wall penetration [see Figure 23(c)]. Similar behavior is observed for surface cracks that have an initial value of  $a/c=1.0$  (TB-3 and TB-5) where the surface crack shape in the experiment slightly deviated from a semi-elliptical shape [see Figure 23(b)]. The deviation of surface crack shape from semi-elliptical does not significantly affect the overall crack growth results (e.g., time to leakage and crack length at leakage predictions). Therefore, although the shape of real fatigue cracks may slightly deviate from semi-elliptical, the use of semi-elliptical surface crack K-solutions to predict the crack growth behavior is reasonable. Hence, the differences between the measured and predicted results shown in Figure 25 for some cases will not have a significant effect on the overall xLPR predictions. Furthermore, the acceptance criterion for surface cracks [Equation 17] was met for all six cases.

Validations of K-solutions for non-idealized and idealized through-wall cracks are provided in Figure 26. In this figure, the through-wall crack shape is represented by the normalized crack angles at the ID and OD surfaces, i.e.,  $\theta_1/\pi$  and  $\theta_2/\pi$ . Note that  $\theta_1=\theta_2$  for an idealized through-wall crack. The prediction results in Figure 26 start from the initial non-idealized through-wall crack determined by the CT Module. As illustrated in this figure, the ID crack angle ( $\theta_1$ ) remains almost constant during the crack transition, whereas the OD crack angle ( $\theta_2$ ) increases until it becomes approximately equal to  $\theta_1$ . Once an idealized through-wall crack is formed ( $\theta_1=\theta_2$ ), the through-wall crack maintains that shape as it continues to grow around the circumference. The predicted results provided good agreement with the experimental results throughout the crack transition stage as well as the idealized through-wall crack growth. In addition, the acceptance criterion for through-wall cracks [Equation 18] was met for all four cases shown in Figure 26.

Figure 27 compares the overall predicted and measured crack front shapes for two example cases. The comparisons are made at an indeterminate number of cycles since the number of cycles between beach marks was not presented in [3]. The crack shape evolutions for surface crack, transitioning crack, and through-wall crack are well captured by the predictions. The differences in the crack front shape for transitioning cracks are due to the shape assumption that was made in the development of the non-idealized through-wall crack K-solutions [8], where the curvature of the non-idealized through-wall crack front was determined from a cylindrical transformation of a straight crack front in a plate (with different crack lengths at the two plate surfaces). However, as demonstrated in Figure 26, the effect of this assumption on the crack angle predictions is negligible. Furthermore, only crack angles are used in the actual xLPR code calculations.

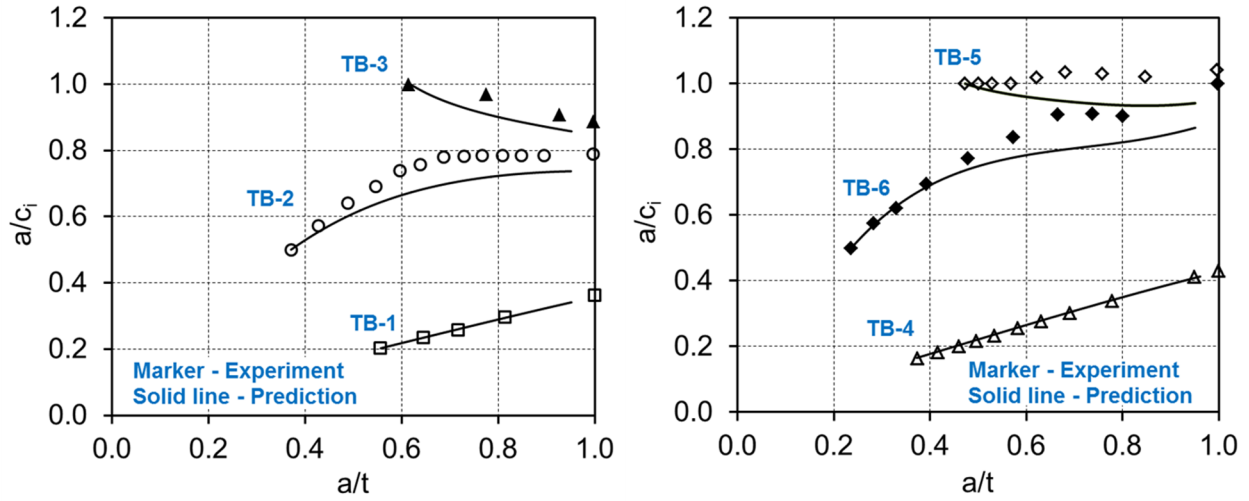


Figure 25. Comparison of surface crack growth

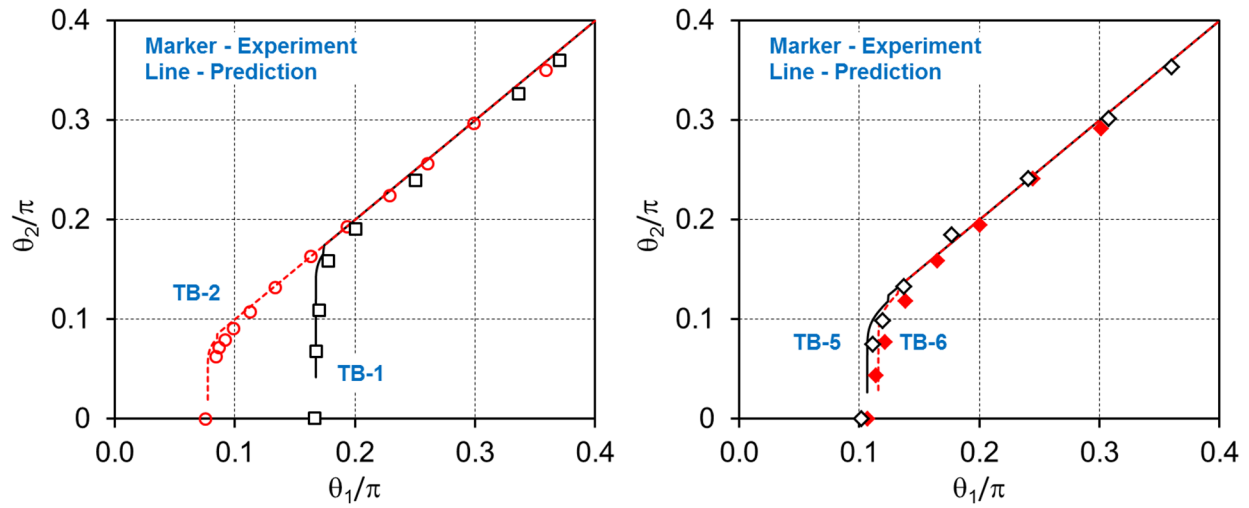


Figure 26. Comparison of crack transition and through-wall crack growth

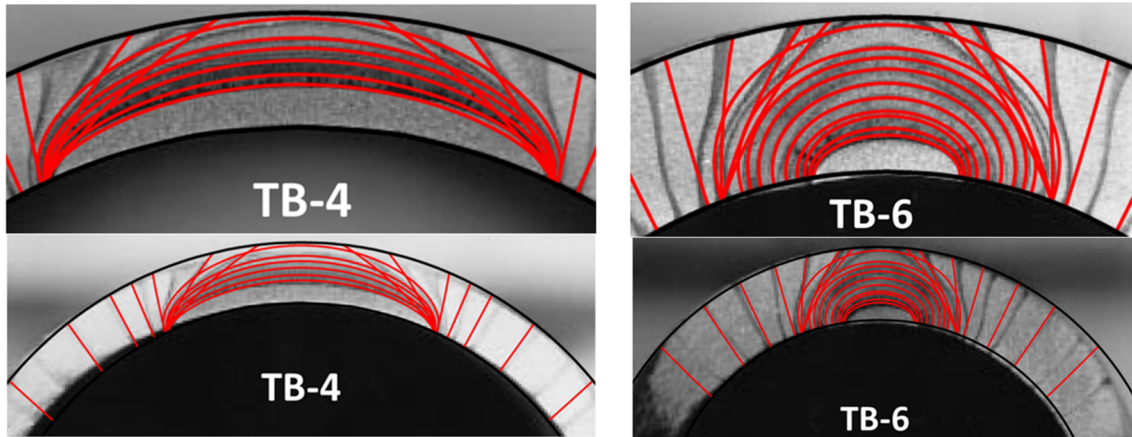


Figure 27. Comparison of predicted and measured crack front shapes during crack growth (at random cycles)

Figure 28 compares the predicted and experimentally measured number of cycles to wall penetration. Experimental data are provided in Table 22. Note that the predictions are based on the FCGR parameters provided in [3]. The calculation over-predicted the experimental results by an average of 37%. This may be due to the less accurate K-solutions that were used in [3] to determine the FCGR. To investigate the effect of FCGR on crack shape evolution, optimized FCGR parameters were determined from the experimental data by changing the C and n values in Equation 16 to make the predicted and measured values align closer to the 1:1 line, as illustrated in Figure 29. Figure 30 demonstrates that the effect of FCGR constants on crack shape evolution for TB-1 is negligible. Similar to TB-1, the crack shape evolution was not affected by the FCGR constants in the other five cases.

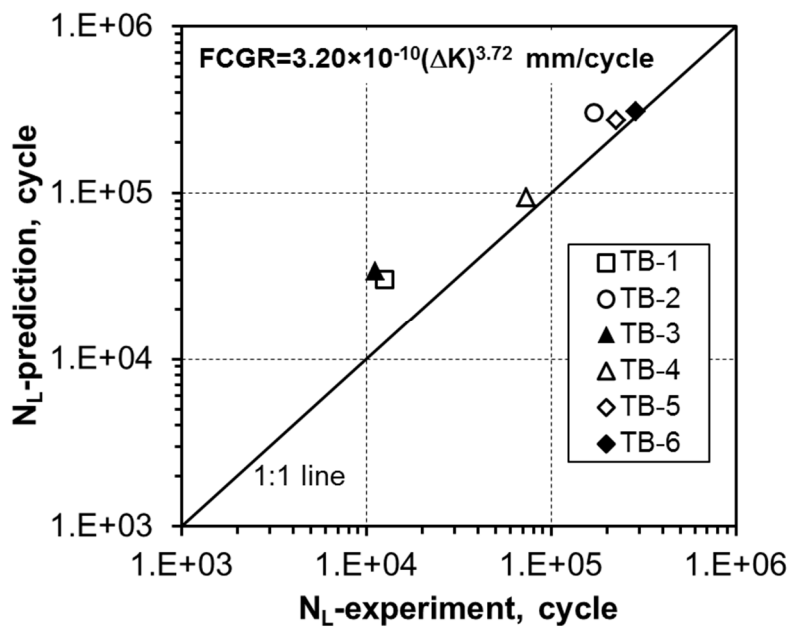


Figure 28. Comparison of number of cycles to wall penetration using FCGR from [3]

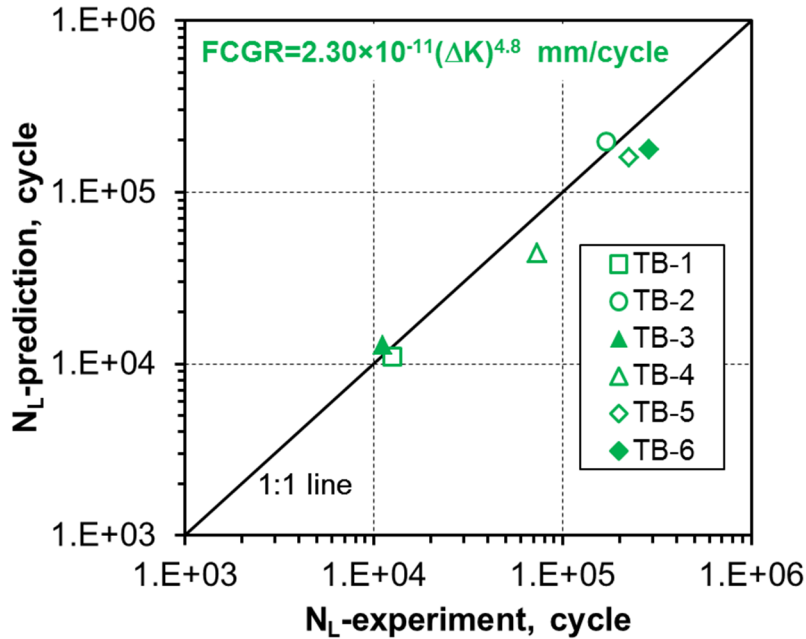


Figure 29. Comparison of number of cycles to wall penetration using optimized FCGR

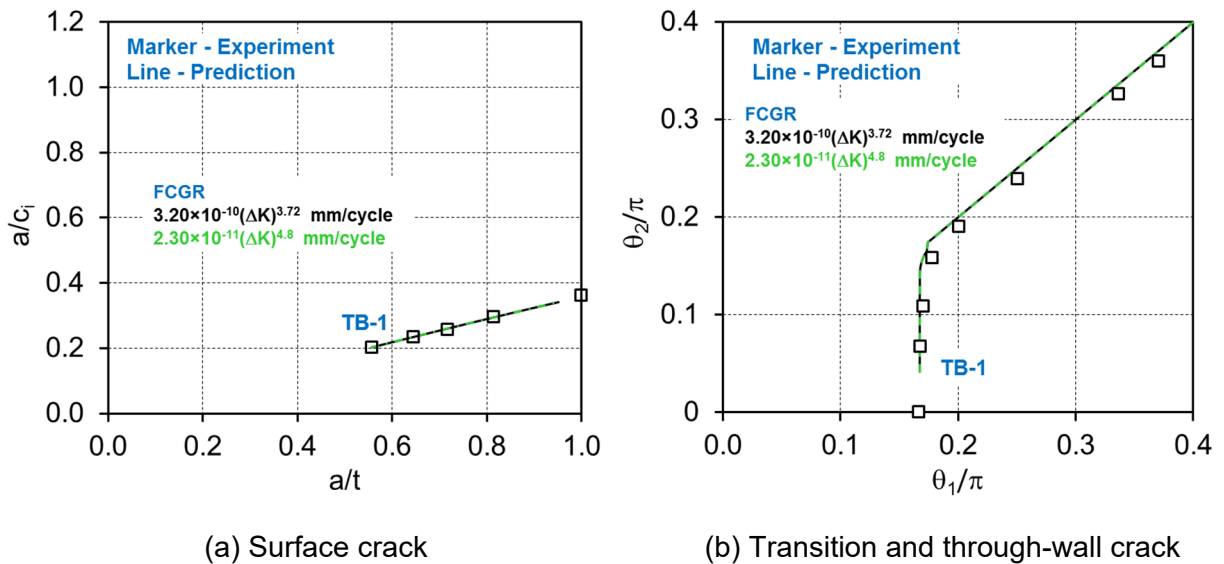


Figure 30. Effect of FCGR on crack growth and crack shape evolution

**Engineering Judgment for Axial Crack K-Solutions and Crack Transition**

The K-solutions and crack transition behavior for axial cracks have not been validated against experimental data since no experimental data exist. However, since K-solutions for all axial cracks (i.e., semi-elliptical surface crack, idealized and non-idealized through-wall cracks) have been developed using the same finite element analysis methods that were used for circumferential cracks, the fidelity of the axial crack K-solutions is expected to be similar to the circumferential crack K-solutions. Furthermore, the axial crack transition rules follow the same rules as the circumferential crack transition [9].

### 3.4 Module Limitations

One of the major enhancements for xLPR Version 2.0 is the addition of the CT Module. However, there still remain a few limitations associated with this module that include:

The correction factors are only available for simple loading conditions (i.e., global bending, axial tension, and internal pressure) and are not available for arbitrary through thickness stress distributions (e.g., weld residual stress; WRS). In xLPR Version 2.0, the effect of WRS is neglected for through-wall cracks (K and COD). However, if future versions of xLPR include the effect of WRS for through-wall cracks, additional correction factors need to be developed.

The correction factors for COD (H values) were developed using linear elastic FE analyses. However, the idealized TWC COD values calculated from the COD modules are elastic-plastic COD values. In xLPR Version 2.0, the elastic correction factors are applied to the elastic-plastic COD values. In order to investigate the effect of plastic deformation on COD, elastic-plastic COD values (and corresponding H values) for circumferential non-idealized TWCs were calculated using FE analyses. The pipe size was fixed to  $R_m/t = 5$  and the ID crack size was fixed to  $\theta_1/\pi = 0.125$  where four different values of  $\theta_1/\theta_2$ , 1, 2, 3 and 4, were considered. For the elastic-plastic material properties, yield strength ( $\sigma_y$ ) of 380 MPa and Ramberg-Osgood parameters of  $\alpha = 1$  and  $n = 5$  were used. For each case, the elastic-plastic COD values were calculated at five different global bending stresses ( $\sigma_b/\sigma_y = 0.2, 0.4, 0.6, 0.8, \text{ and } 1.0$ ). Figure 31 shows the corresponding H values calculated from the elastic-plastic COD values for various global bending stress values. The circle marks are the H values determined from the linear elastic FE analyses, which are currently used in the CT Module. As illustrated in this figure, for relatively low global bending stresses, the elastic and elastic-plastic H values show small differences. However, as the global bending stress increases, the elastic-plastic  $H_1$  values decrease and the elastic-plastic  $H_2$  values slightly increase compared to the elastic H values. This implies that the ID COD values will be overestimated and the OD COD values will be slightly underestimated when elastic H values are used for elastic-plastic COD estimations in xLPR. The overall effects on leak rate calculations have not been investigated in this effort and the uncertainty should be investigated.

Table 23 summarizes the CT Model/Module assumptions and xLPR implications.

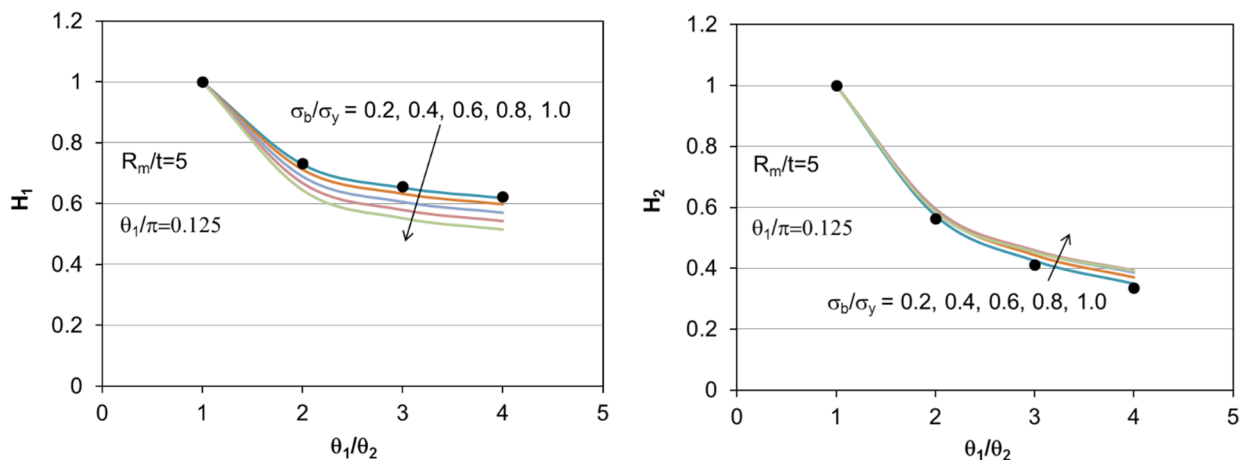


Figure 31. Effect of plastic deformation on COD correction factor (H) values

**Table 23. Summary of CT Model/Module assumptions and xLPR implications**

<b>Model / Module Assumptions</b>	<b>Implications</b>	<b>Expected Contribution to Module Prediction or xLPR Result Bias</b>
<p>Partial ellipse crack front shapes were assumed to best represent the natural crack shape transition.</p>	<p>This shape was assumed for model simplification and because results demonstrated that the partial semi-ellipse well-represented the progression of the crack front shape throughout transition.</p>	<p>Minor impact on module prediction bias expected to result from this assumption as demonstrated in this report.</p>
<p>Crack transition is assumed to begin once the surface crack depth reaches 95% of the wall thickness.</p>	<p>This assumption is made since the surface crack K solutions are valid for up to crack depth of 95% of the wall thickness. In addition, this criterion was developed from experimental results where the load levels were sufficiently low to prevent significant ductile tearing.</p>	<p>This assumption is expected to result in a slightly earlier prediction of time to wall penetration. However, as demonstrated in this report, the overall effect of this assumption on the crack transition behavior is negligible.</p>
<p>A simple crack morphology with no engagement across the crack faces (unlike PWSCC) is assumed for the COD analyses.</p>	<p>This assumption is made for model simplification and to be consistent with how the COD module was developed. PWSCC cracks are expected to have a structure similar to a porous medium, with ligaments constraining crack shape development.</p>	<p>The COD correction factors are not affected by this assumption since it is a normalized parameter. The uncertainties associated with this assumption should be characterized in the COD module.</p>
<p>Linear elasticity was assumed for development of correction factors for COD (H values).</p>	<p>As the applied stress increase, ID COD values will tend to be overestimated and the OD COD values will be slightly underestimated when elastic H values are used for elastic-plastic COD estimations in xLPR.</p>	<p>The overestimated and underestimated ID and OD COD values, respectively, will somewhat compensate each other in the leak rate calculations. However, the overall effects on leak rate calculations should be investigated to quantify the uncertainty.</p>

#### **4. RECOMMENDATIONS FOR VERSION 3.0 MODIFICATIONS**

If future versions of xLPR include the effect of WRS for through-wall cracks, additional correction factors need to be developed for non-idealized through-wall cracks (both circumferential and axial) to capture the arbitrary through thickness stress distributions. This may require a large number of finite element analyses.

The effect of plastic deformation on the COD correction factors (H values) should be investigated to determine if the elastic correction factors are sufficient and also to determine the uncertainty in the leak rate calculations.

## **5. LESSONS LEARNED**

The following list provides the significant findings from the CT Module development process:

- By applying correction factors to the K and COD values of idealized through-wall cracks, it was possible to model non-idealized through-wall cracks.
- Based on the FE calculation results, it was demonstrated that the correction factors for K (G values) were sensitive to the number of elements through the pipe wall thickness, whereas the correction factors for COD (H values) were not.
- The criteria used to determine the onset of crack transition and the initial non-idealized crack size was adequate to capture the natural crack transition from the referenced experiment.
- The crack front shape of the non-idealized crack can affect the K values at the inner and outer surfaces. The crack front shapes assumed in the crack transition model were sufficient to mimic the experimental results.
- Crack shape evolution during crack growth (including crack transition) is independent of the crack growth rate.

## **6. SUMMARY**

A surface to through-wall crack transition model has been developed using K and COD solutions for non-idealized through-wall cracks. As part of the xLPR Ver. 2.0 development, the existing K and COD solutions for non-idealized circumferential TWC were updated and expanded. First, a mesh sensitivity study (which was not conducted in the previous work) was carried out to determine the appropriate mesh size required to accurately calculate the K and COD values. Then, finite element analyses were performed to recalculate the correction factors for the non-idealized TWCs. For axial cracks, a study was conducted to define the appropriate crack front shape for non-idealized axial TWCs using natural crack growth simulations. After examining the natural crack shapes, new solutions were developed using the partial ellipse crack front shapes.

The K and COD values for non-idealized TWCs were represented by applying correction factors to solutions for idealized TWCs with the same ID crack size. These correction factors were utilized in the crack transition model.

The crack transition model includes a criterion for transitioning the final surface crack to the initial non-idealized through-wall crack which determines when the transition should occur (based on surface crack depth) and determines the two crack lengths (at ID and OD surfaces) of the initial non-idealized through-wall crack. Furthermore non-idealized through-wall crack growth can be conducted using the model.

The xLPR Ver. 2.0 CT Module was developed using the crack transition model. The module was developed according to the CT SRD and CT SDD. Verification of the CT Module was carried out according to the CT STP. The verification of the CT Module is documented in detail in the CT STRR. The testing activity described in the STRR verified that the requirements specified in the CT SRD were met.

Finally, the CT Module was validated by comparing the crack growth calculation results with experimental data from the literature. The CT Module and other modules (K modules) were used to simulate fatigue crack growth of circumferential cracks in pipes under bending up to wall penetration and to through-wall crack transition stage until idealized through-wall cracks were formed. The validation was focused on the crack shape evolution during the crack growth. The crack sizes/shapes formed during the crack growth were well captured by the xLPR modules. This also validated that the crack shapes used in xLPR (i.e., semi-elliptical surface crack, non-idealized through-wall crack, and idealized through-wall crack) are sufficient to represent the crack shapes formed during laboratory pipe fatigue tests. Furthermore, by demonstrating that the crack shape evolution is independent of FCGR, the accuracy of the K-solutions was validated.

## 7. REFERENCES

1. Rudland, D., Csontos, A., and Shim, D.J., “Stress Corrosion Crack Shape Development Using AFEA,” ASME Journal of Pressure Vessel Technology, Vol. 132(1), 011406, 2010.
2. Shim, D.J., Rudland, D., Harris, D., “Modeling of Subcritical Crack Growth Due to Stress Corrosion Cracking – Transition from Surface Crack to Through-Wall Crack,” PVP2011-57267, Proceedings of the 2011 ASME Pressure Vessels and Piping Conference, July 17-21, 2011, Baltimore, Maryland, USA.
3. Yoo, Y.S., Ando, K., “Circumferential Inner Fatigue Crack Growth and Prediction Behaviour in Pipe Subjected to a Bending Moment,” Fatigue and Fracture of Engineering Materials and Structures, Vol. 23, pp. 1-8, 2000.
4. Rudland, D., Harrington, C., “Extremely Low Probability of Rupture (xLPR) Version 1.0 Code – Pilot Study Problem Results,” PVP2011-57531, Proceedings of the 2011 ASME Pressure Vessels and Piping Conference, July 17-21, 2011, Baltimore, Maryland, USA.
5. Huh, N.S., Shim, D.J., Choi, S., Wilkowski, G., Yang, J.S., “Stress Intensity Factors for Slanted Through-Wall Cracks Based on Elastic Finite Element Analyses,” Fatigue and Fracture of Engineering Materials and Structures, Vol. 31(2), pp.197-209, 2008.
6. Huh, N.S., Shim, D.J., Choi, S., Park, K.B., “Stress Intensity Factors and Crack Opening Displacements for Slanted Axial Through-Wall Cracks in Pressurized Pipes,” Fatigue and Fracture of Engineering Materials and Structures, Vol. 31(6), pp. 428-440, 2008.
7. Huh, N.S. Huh, Shim, D.J., Yoo, Y.S., Choi, S., Park, K.B., “Estimates of Elastic Crack Opening Displacements of Slanted Through-Wall Cracks in Plate and Cylinder,” ASME Journal of Pressure Vessel Technology, Vol. 132(2), 021401, 2010.
8. Shim, D.J. Shim, Park, J.S., Rudland, D., “Surface to Through-Wall Crack Transition Model for Circumferential Cracks in Pipes,” Fatigue and Fracture of Engineering Materials and Structures, Submitted for publication, 2015.
9. Shim, D.J. Shim, Park, J.S., Rudland, D., “Non-Idealized Surface to Through-Wall Crack Transition Model for Axial Cracks in Cylinders,” ASME Journal of Pressure Vessel Technology, Vol. 138(1), 011203, 2016.
10. Zahoor, A, “Ductile Fracture Handbook,” Electric Power Research Institute, Palo Alto, California, 1991.
11. American Petroleum Institute and American Society of Mechanical Engineers, “Fitness-for-Service, API 579-1/ASME FFS-1,” API 579 Second Edition, 2007.
12. Shim, D.J., Xu, S. and Lee, D., “Closed-Form Stress Intensity Factor Solutions for Circumferential Through-Wall Cracks in Cylinder,” PVP2014-28049, Proceedings of the 2014 ASME Pressure Vessels and Piping Conference, July 20-24, 2014, Anaheim, California, USA.
13. Yoo, Y.S., “Crack Opening Displacement of Circumferential Through-Wall Cracked Cylinders Subjected to Tensile and Through-Wall Bending Loads,” Nuclear Engineering and Design, Vol 229, pp. 123-138, 2004.

14. ABAQUS, User's Manual, Version 6-13.2, SIMULIA, Providence, USA, 2014.
15. British Energy Generation Ltd., R6: Assessment of the integrity of structures containing defects. Revision 4, III.11.1–III.11.42., 2001.
16. xLPR-SRD-CTM, xLPR Software Requirements Description for Crack Transition Module, Version 2.1, September, 2015.
17. xLPR-SDD-CTM, xLPR Software Design Description for Crack Transition Module, Version 2.1, September, 2015.
18. xLPR-STP-CTM, xLPR Software Test Plan for Crack Transition Module, Version 1.1, September, 2015.
19. xLPR-STRR-CTM, xLPR Software Test Results Report for Crack Transition Module, Version 1.1, October, 2015.
20. xLPR-MVR-K\_CTM, xLPR Module Validation Report for K Solution and Crack Transition Modules, Version 1.0, May, 2015.
21. Version 1.0 of the Crack Transition Module Fortran source code including the driver, "ctm\_driver\_version1.f90" in Subversion directory - \xldr\tags\xLPR-CTM\Crack\_Transition
22. Williams, P. T., "Recommended Programming Practices and Standards for Developing xLPR Modules Using Fortran," ORNL/TM-2013/64, Oak Ridge National Laboratory, Oak Ridge, TN, August 2013.
23. Yoo, Y.S., Ahn, S.H., Ando, K., "Fatigue Crack Growth and Penetration Behaviours in Pipes Subjected to Bending Moment" Proceedings of the 1998 ASME Pressure Vessels and Piping Conference, PVP-Vol. 371, High Pressure Technology, pp 63-70, 1998.
24. Newman, J.C. and Raju, I.S., "An Empirical Stress Intensity Factor Equation for the Surface Crack," Engineering Fracture Mechanics, Vol. 15, pp. 185-192, 1981.
25. xLPR-STRR-KPW, xLPR Software Test Results Report for K Calculator for Circumferential and Axial Part-Through-Wall Cracks, Version 1, December, 2014.
26. xLPR-STRR-KTW, xLPR Software Test Results Report for K Calculator for Circumferential and Axial Through-Wall Cracks, Version 1, February, 2015.